# Target recognition and preferential degradation of toxic chemical groups by innovative group-imprinted photocatalyst with footprint cavity

Junlong Peng, Fang Deng [*], Hongxin Shi, Zhenzhou Wang, Xibao Li, Jianping Zou, Xubiao Luo

*National-Local Joint Engineering Research Center of Heavy Metal Pollutants Control and Resource utilization, Nanchang Hangkong University, Nanchang 330063, PR China*

## A R T I C L E   I N F O

## A B S T R A C T

Target recognition and preferential degradation of toxic chemical groups remain critical challenges in photocatalytic degradation of organic contaminant. In this study, the concept of group-imprinting was first proposed, and group-imprinted copolymers of aniline and pyrrole were grafted from the surface of magnetic $CuFeO_2@MnO_2$ nanocomposites ($MIP$-$CuFeO_2@MnO_2$) using acrylamide as dummy templates for imprinting the amide group of tetracycline for the first attempt, and the molar ratios of dummy template molecule to functional monomer was optimized. The magnetic $MIP$-$CuFeO_2@MnO_2$ showed high adsorption capacity and good recognition for tetracycline. In mixture solution of tetracycline and ibuprofen, the distribution coefficient ($k_d$) value of $MIP$-$CuFeO_2@MnO_2$ for tetracycline was 0.308 L/g, which is 6.86 times more than for ibuprofen (only 0.045 L/g). The selection factor ($\alpha$) of $MIP$-$CuFeO_2@MnO_2$ is about 3.2 times that of non-imprinted counterpart, indicating that the imprinting cavities in copolymer layer which match with the amide groups of tetracycline can selectively recognize and adsorb tetracycline. More importantly, $MIP$-$CuFeO_2@MnO_2$ exhibited preferential degradation performance for amide groups, which was confirmed by the intermediates and degradation pathway. The *E. coli* growth suggests effective toxicity reduction of tetracycline due to the preferential degradation of amide groups by photocatalysis of $MIP$-$CuFeO_2@MnO_2$.

## 1. Introduction

With mass production and the extensive use of antibiotics in human medical treatment and animal husbandry, massive antibiotics have been released into natural water environment [1,2]. The presence of antibiotics in natural water even at trace level poses a long-term risk and negative impact to environmental ecosystems and human health, which is attributed to some toxic pharmacophoric groups in molecular structure of antibiotics [3,4]. The toxic pharmacophoric groups usually lack of electrons and have the electrophilic nature, thus can react with nucleophilic centers in nucleic acids, proteins or other important components in the body [5], causing irreversible damage to the body [6]. Therefore, how to remove antibiotics from water, especially how to preferentially destroy the toxic pharmacophoric groups of antibiotics, has become an urgent problem [7].

The common treatment methods of antibiotics in water mainly include adsorption [8–10], membrane treatment technology [11–13], electrochemical treatment [14,15], activated sludge method [16,17], ozonation, Fenton catalytic oxidation, chlorination, and other advanced oxidation processes [18–20]. Although these methods can remove antibiotics from water, they still have some shortcomings such as high operation cost, the formation of more toxic by-products, secondary pollution and high energy consumption [21]. Photocatalysis oxidation technology has promising prospect in water treatment in virtue of high treatment efficiency, easy control of operating conditions, simple process equipment, easy availability of catalytic materials, no secondary pollution, and direct use of sunlight [22–25]. To date, many photocatalysts such as $CuFeO_2$, $MnO_2$ and their composites have been fabricated for degradation of antibiotics. $CuFeO_2$ is attractive because of its suitable band structure, simple synthesis, high chemical stability, low toxicity, low cost, good visible-light absorption, high photocatalytic activity, and easy magnetic recycling. The unique properties of manganese dioxide ($MnO_2$) such as acid resistance, low cost, narrow bandgap, low toxicity, and high environmental compatibility make it a promising in environmental purification. The combination of magnetic $CuFeO_2$ and $MnO_2$ not only integrate their own advantages, but only can be magnetically recovered. The relevant studies mainly focus on the development of photocatalytic materials and performance evaluation

---

from the perspective of degradation rate, COD and TOC removal [26, 27]. However, these indicators cannot reflect the degradation of toxic pharmacophoric groups in antibiotic molecules. More importantly, photocatalytic degradation of organic pollutants is not selective, and reactive species such as hydroxyl radicals (•OH) cannot selectively and preferentially destroy the pharmacophoric groups of antibiotics. Therefore, the selectivity improvement of photocatalysts is of scientific and practical significance.

Much effort has been made to improve the photocatalytic selectivity, such as regulation of surface charge state [28], the modification of the catalyst surface with special small molecules [29], the design of photocatalysts with selective adsorption region and a photocatalysis-active region, and catalysts with exposed specific crystal planes [30]. Although these methods can selectively adsorb and degrade target pollutants to a certain extent, they still lack specific recognition sites, and suffer from insufficient degradation selectivity. Molecular imprinting is a promising tailored method to obtain synthesized material with specific recognition ability and adsorption selectivity for target molecules. The coupling of molecular imprinting with photocatalysis technology can enhance the photocatalytic selectivity for template molecules, however, the molecularly imprinted photocatalysts cannot selectively and preferentially destroy the specific chemical groups of organic pollutants, resulting in unsatisfactory toxicity reduction. Therefore, it is still urgent to design a novel group-imprinted photocatalyst with strong targeted binding and selective degradation ability for specific chemical groups of organic pollutants.

In this study, the concept of group-imprinting was first proposed, and a novel group-imprinted copolymer layer was constructed on the surface of CuFeO$_2$@MnO$_2$ (MIP-CuFeO$_2$@MnO$_2$) using aniline and pyrrole as functional monomers, acrylamide as dummy templates for imprinting the amide groups of tetracycline for the first attempt, and the molar ratios of dummy template molecule to functional monomer were optimized. The group imprinted polymer layer contains a large number of imprinted cavities that can match well with the size, shape and charge of the amide groups of tetracycline, thus MIP-CuFeO$_2$@MnO$_2$ is expected to show target recognition and photocatalytic selectivity for pharmacophoric groups. The adsorption kinetics and isotherms, and adsorption selectivity of MIP-CuFeO$_2$@MnO$_2$ were studied. Most importantly, the photocatalytic selectivity of MIP-CuFeO$_2$@MnO$_2$ for preferential degradation of amide groups in tetracycline was explored.

## 2. Experimental

### 2.1. Preparation of MIP-CuFeO$_2$@MnO$_2$

#### 2.1.1. Preparation of CuFeO$_2$@MnO$_2$

0.375 g home-made CuFeO$_2$ (Supporting information) was dispersed in 50 mL ultrapure water, and was sonicated for 10 min, and then 0.675 g KMnO$_4$ and 1.5 mL HCl (3.9 mol/L) was successively added into the above suspension under vigorous stirring, and the stirring was lasted for another 20 min. The mixture reacted in 100 mL Teflon-lined autoclave reactor at 180 °C for 12 h. After natural cooling, washing and drying, CuFeO$_2$@MnO$_2$ was obtained [31,32].

#### 2.1.2. Preparation of MIP-CuFeO$_2$@MnO$_2$

1.5 g CuFeO$_2$@MnO$_2$ was dispersed in 40 mL acetonitrile, and ultrasonicated for 10 min (labelled as A). 2.2 mL aniline and 1.66 mL pyrrole (the molar ratio of aniline to pyrrole is 1:1) were dissolved in 10 mL acetonitrile and ultrasonicated for 10 min, then different amount of acrylamide was added, and stirred for 4 h to form preassembly solution (labelled as B) [33]. The dispersion A and preassembly solution B were mixed. 0.3 g of ammonium persulfate as the initiator was ultrasonically dissolved in 10 mL of ultrapure water, and was added dropwise to the above mixture. After polymerization reaction for 4 h, the solid was purified with ammonia solution: methanol (1:1, v/v) in a Soxhlet extractor until acrylamide was not detected in the elution solution, and

finally was washed with methanol and ultrapure water. The product was referred to as MIP-CuFeO$_2$@MnO$_2$. For comparison, the copolymer layer of aniline and pyrrole was constructed on the surface of CuFeO$_2$@MnO$_2$ (PANI/PPy-CuFeO$_2$@MnO$_2$), and this non-imprinted PANI/PPy-CuFeO$_2$@MnO$_2$ photocatalyst was prepared using the same procedure as MIP-CuFeO$_2$@MnO$_2$ but without adding acrylamide, which was referred to as NIP-CuFeO$_2$@MnO$_2$.

### 2.2. Adsorption experiment

The adsorption kinetics for tetracycline (TC) was carried out by dispersing 50 mg of NIP-CuFeO$_2$@MnO$_2$ or MIP-CuFeO$_2$@MnO$_2$ was dispersed in 100 mL of TC solution (10 mg/L) under magnetic stirring in the dark. The suspension was sampled at 3 min intervals, and was immediately filtered with 0.22 μm membrane. The absorbance of filtrate was measured with ultraviolet-visible spectrophotometer at 367 nm [34], and the concentration of residual TC in filtrate was obtained by Lambert-Beer law.

The adsorption isotherms were performed for 12 h in an incubator shaker with an oscillation rate of 180 rpm at 25 ± 0.1 °C. 50 mg of MIP-CuFeO$_2$@MnO$_2$ or NIP-CuFeO$_2$@MnO$_2$ was dispersed in 50 mL tetracycline solution with initial TC concentration in range of 2 ∼ 50 mg/L. Then the dispersion was filtered with 0.22 μm membrane, and the residual TC concentration was analyzed by with ultraviolet-visible spectrophotometer at 367 nm. The equilibrium adsorption capacity ($Q_e$) was calculated according to the following equation:

$$Q_e = \frac{(C_0 - C_e)V}{m}$$

where $C_0$, $C_e$ (mg/L) and $V$ (L) are the initial concentration, equilibrium concentration and volume of TC solution, respectively; and $m$ (g) is the weight of the catalyst [35].

Adsorption selectivity of MIP-CuFeO$_2$@MnO$_2$ was investigated in a 100 mL of binary mixture solution of TC and ibuprofen (IBP) with individual initial concentrations of 10 mg/L. After adsorption equilibrium, the supernatant was collected and the residual concentration was analyzed by high performance liquid chromatography (HPLC) [36]. The distribution coefficient ($k_d$) and selectivity coefficient ($\alpha$) were utilized to evaluate the recognition selectivity of MIP-CuFeO$_2$@MnO$_2$ and MIP-CuFeO$_2$@MnO$_2$, which were calculated as followed:

$$k_d = \frac{(C_0 - C_e)V}{mC_e}$$

$$\alpha = \frac{k_{d1}}{k_{d2}}$$

where $Q_e$ (mg) is the adsorption amounts of catalysts and $C_e$ (mg/L) is the equilibrium concentration of the solution. where $k_{d1}$ and $k_{d2}$ are the distribution coefficient for TC and IBP as competing molecules, respectively. The $\alpha$ is the ratio of $k_{d1}$ to $k_{d2}$ in the mixture solution.

### 2.3. Photocatalytic activities and stability

In the photodegradation experiment, 0.05 g of MIP-CuFeO$_2$@MnO$_2$, NIP-CuFeO$_2$@MnO$_2$ or CuFeO$_2$@MnO$_2$ was dispersed in 100 mL TC solution (10 mg/L) under continuous magnetic stirring. After reaching the adsorption-desorption equilibrium, the 300 W xenon lamp (Microsolar300, Beijing Perfectlight) was utilized as the source of visible light (λ > 400 nm) to irradiate the solution, and 5 mL of the tetracycline solution was sampled at specific interval of 20 min and immediately filtered. The residual TC concentrations were monitored by ultraviolet-visible spectrophotometer. The degradation intermediate products were identified using high performance liquid chromatography-mass spectrometry (HPLC-MS).

The active species in photocatalytic degradation of TC were trapped

by adding isopropanol (IPA), triethanolamine (TEOA), and p-benzo-quinone (BQ) to the photocatalytic system as scavengers of hydroxyl radicals ($\cdot$OH), $h^+$, and superoxide radicals ($O_2^{\cdot-}$), respectively [37]. The experimental conditions were the same as the photocatalytic degradation of TC by MIP-CuFeO$_2$@MnO$_2$.

The stability was studied by magnetic recovery of MIP-CuFeO$_2$@MnO$_2$ from the suspension, and repeated for subsequent cycle in TC degradation.
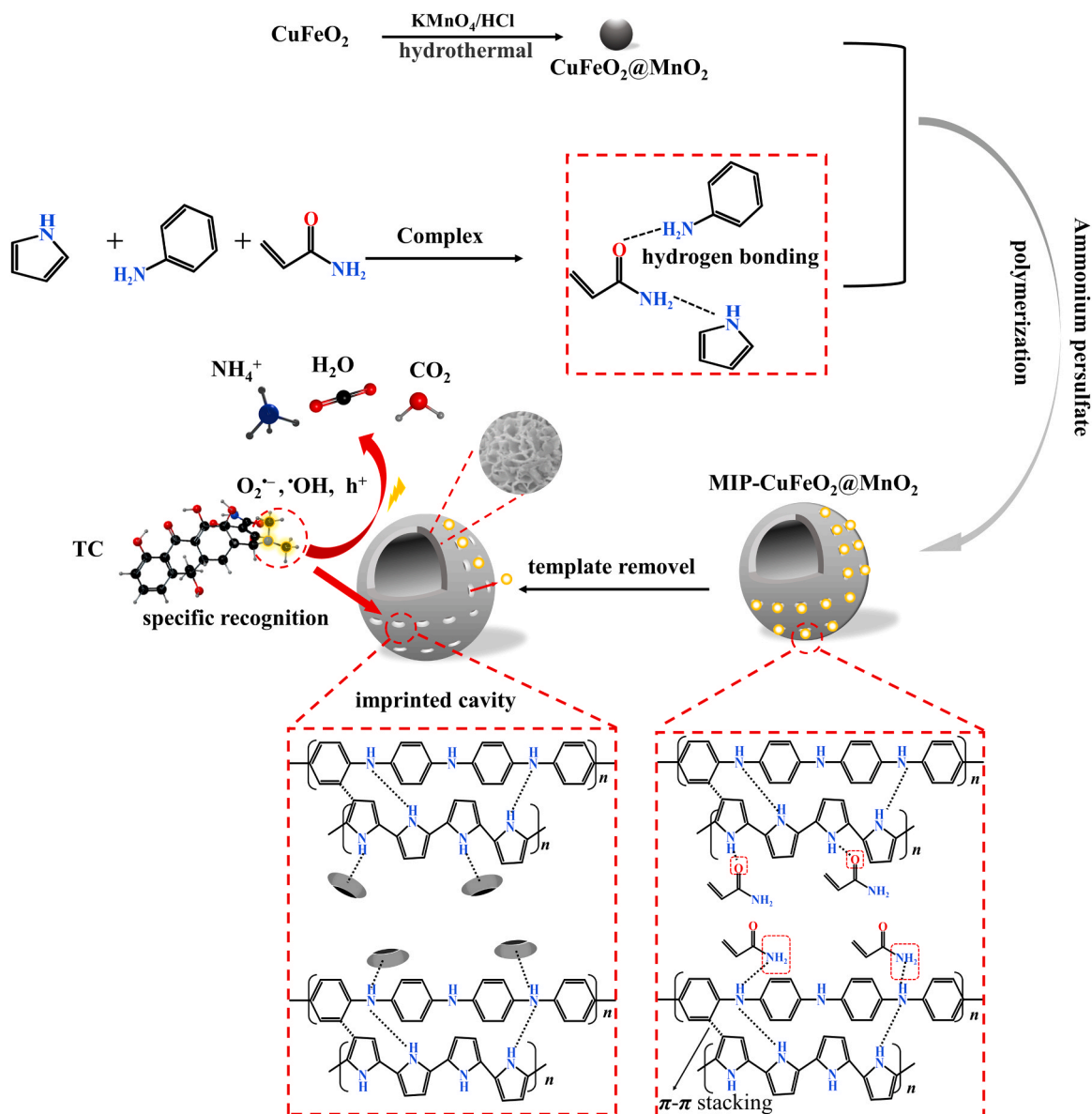
### 2.4. Biological toxicity of TC and intermediate products

The biological toxicity of TC and intermediate products was evaluated by growth curve of *E. coli* in liquid medium. The experimental operation for growth curve of *E. coli* in liquid medium is as follows: 5 g beef extract, 5 g NaCl and 10 g peptone were well mixed with 1000 mL deionized water to obtain liquid medium. 50 mL of liquid medium, 10 mL TC solution or 10 mL of intermediate solution and 5 μL of the second-generation *Escherichia coli* were added in the sterilized Erlenmeyer flask. Then the Erlenmeyer flasks were sealed with parafilm, and placed in a shaking incubator at 30 °C. About 3 mL bacterial solution

was taken out at different culture time, and the absorbance was measured at 600 nm to evaluate the *E. coli* growth. Similarly, the control experiment was performed with LB liquid medium alone.

### 2.5. Density functional theory (DFT) calculation

All the DFT calculations were performed by using Gaussian 16 package. The geometries optimizations were computed by employing the B3LYP functional with 6–311 G(d) basis set. The Grimme's DFT-D3 with BJ-damping method was applied to correct the van der Waals interaction. The analysis of electronic structure was performed by using Multiwfn 3.8 (dev) code. The isosurface maps of real space functions were rendered by means of Visual Molecular Dynamics (VMD) software based on the files exported by Multiwfn. The isosurface of Fukui function was set to 0.005. The interaction energy ($E_{int}$) was computed to measure the binding strength of MIP-CuFeO$_2$@MnO$_2$ and tetracycline. It was defined as the energy difference between the MIP-CuFeO$_2$@MnO$_2$ and tetracycline complexed system ($E_{AB}$) and the summation of isolated MIP-CuFeO$_2$@MnO$_2$ ($E_A$) and tetracycline molecule ($E_B$). It can be expressed as $E_{int} = E_{AB} - E_A - E_B$.



**Scheme 1.** Illustration for the preparation of MIP-CuFeO$_2$ @MnO$_2$.

## 3. Results and discussion

### 3.1. Synthesis and characterization of the catalyst

The synthesis route of MIP-CuFeO$_2$@MnO$_2$ with footprint cavities is illustrated in Scheme 1. To realize the efficient recognition of toxic chemical groups, acrylamide was selected as the dummy template molecule for imprinting the amide groups of tetracycline for the first attempt due to the fact that both tetracycline and acrylamide contain amide groups (Fig. S1). Firstly, CuFeO$_2$@MnO$_2$ was produced via two steps. Then, a precursor between the pyrrole, aniline and acrylamide was formed due to electrostatic interaction, hydrogen bonding, π-bonding complexation, which was necessary for a high quality of organic group-imprinted copolymer layer of pyrrole and aniline. With the initiation of ammonium persulfate, the group imprinted copolymer layer was prepared by the polymerization of pyrrole and aniline, and grafted onto the surface of CuFeO$_2$@MnO$_2$. Finally, acrylamide molecules were completely removed from the organic copolymer layer by Soxhlet extraction method, leaving the footprint cavities in the organic copolymer layer to obtain group imprinted MIP-CuFeO$_2$@MnO$_2$. The footprint cavities are expected to be complementary matching with amide groups of tetracycline in spatial configuration and chemical
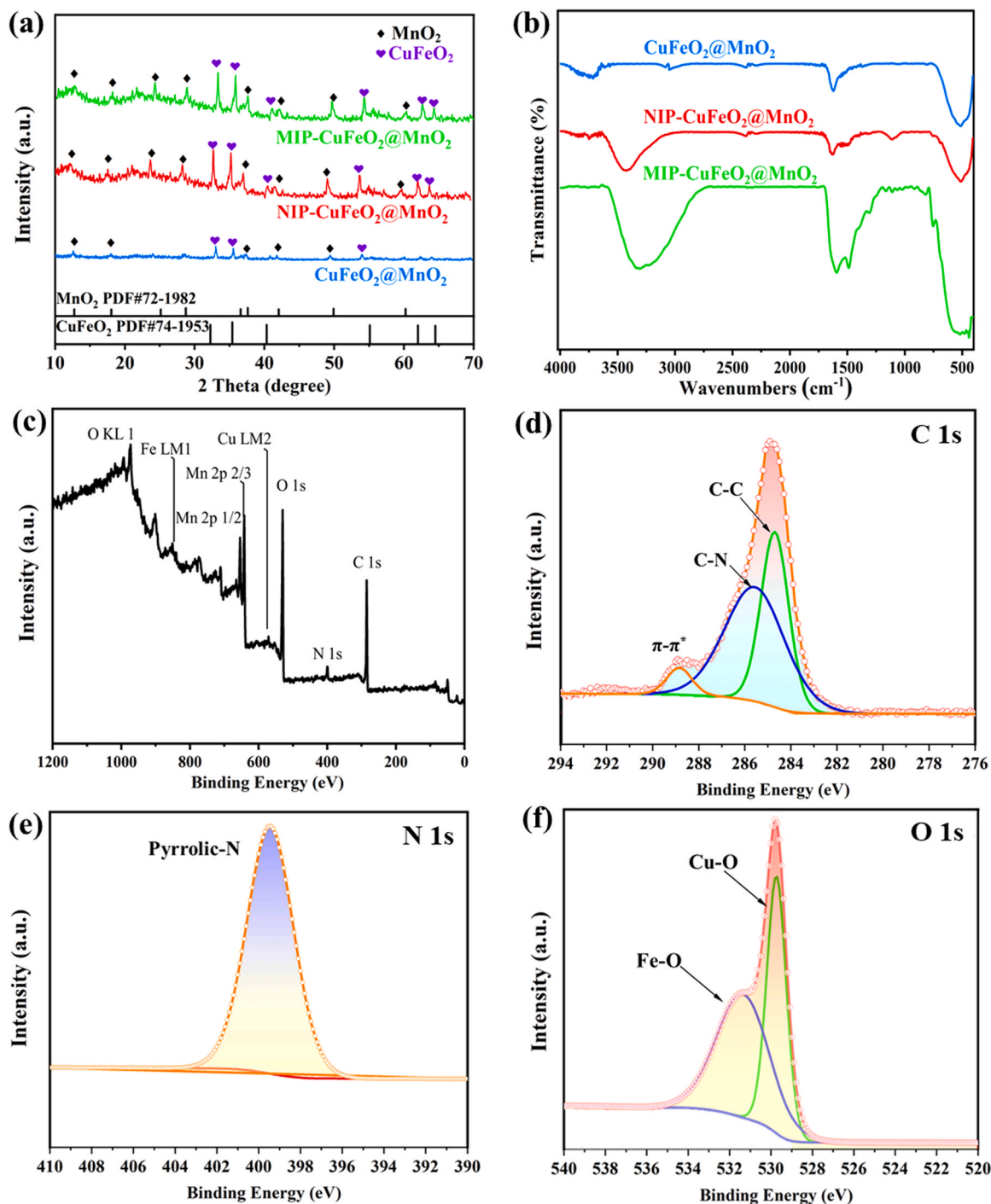


**Fig. 1.** (a) XRD patterns and (b) FT-IR of MIP-CuFeO$_2$@MnO$_2$, NIP-CuFeO$_2$@MnO$_2$ and CuFeO$_2$@MnO$_2$; XPS spectra of MIP-CuFeO$_2$@MnO$_2$: (c) survey spectra, (d) C 1 s, (e) N 1 s, (f) O 1 s.

binding.

The XRD patterns of CuFeO$_2$@MnO$_2$, NIP-CuFeO$_2$@MnO$_2$ and MIP-CuFeO$_2$@MnO$_2$ are shown in Fig. 1a. The diffraction peaks of both CuFeO$_2$ and MnO$_2$ were detected simultaneously in the XRD patterns of CuFeO$_2$@MnO$_2$. The diffraction peaks at 2θ= 31.37°, 35.79°, 40.32° and 55.42° can be indexed to the Bragg reflections from (222), (110), (112) and (233) crystal planes of rhombohedral CuFeO$_2$, and the diffraction peak at 2θ= 12.744°, 18.061°, 36.591°, 42.035° and 49.895° was indexed to the (111), (200), (400), (301) and (411) crystal plane of tetragonal α-MnO$_2$ (JCPDS card No.72–1982). Compared with the CuFeO$_2$@MnO$_2$, the diffraction peak intensity of NIP-CuFeO$_2$@MnO$_2$ and MIP-CuFeO$_2$@MnO$_2$ was enhanced, indicating higher degree of crystallinity [38].

Fourier-transform infrared spectroscopy (FT-IR) of CuFeO$_2$@MnO$_2$, NIP-CuFeO$_2$@MnO$_2$ and MIP-CuFeO$_2$@MnO$_2$ are represented in Fig. 1b. In the FT-IR of CuFeO$_2$@MnO$_2$, the peaks at about 500 cm$^{-1}$ were assigned to the characteristic skeletal vibrations of Fe-O and Mn-O bond, and the peak at 1620 cm$^{-1}$ belonged to skeletal vibration of Cu-O bond. Compared to CuFeO$_2$@MnO$_2$, the absorption band of Fe-O and Cu-O in NIP-CuFeO$_2$@MnO$_2$ and MIP-CuFeO$_2$@MnO$_2$ is red-shifted, and the characteristic structure of aniline-pyrrole copolymer was observed. The shift of Fe-O and Cu-O absorption band in NIP-CuFeO$_2$@MnO$_2$ and MIP-CuFeO$_2$@MnO$_2$ indicates the interaction between the CuFeO$_2$@MnO$_2$ and the aniline-pyrrole copolymer. This interaction was favorable for the electron transport between CuFeO$_2$@MnO$_2$ and the aniline-pyrrole copolymer via the -O- bonds [39]. The absorption peaks at 1558 and 1495 cm$^{-1}$ are assigned to C=C stretching vibration and the C-N stretching vibration, respectively. The absorption band at 3000–3500 cm$^{-1}$ belonged to the hydrogen bonds, indicating that the organic copolymer of aniline and pyrrole was successfully coated on CuFeO$_2$@MnO$_2$ surface [40].

In XPS survey spectrum of MIP-CuFeO$_2$@MnO$_2$, the peaks of Cu, Fe, Mn, O, C, and N elements were observed (Fig. 1c), and element distribution information for both NIP-CuFeO$_2$@MnO$_2$ and MIP-CuFeO$_2$@MnO$_2$ were shown in Table S1. The binding energies at 858.21, 655.83, 643.72 and 587.05 eV belong to Fe LM1, Mn 2p$_{1/2}$, Mn 2p$_{2/3}$ and Cu LM2, respectively. In the C1s spectrum, the peaks at 284.63 and 285.70 eV correspond to the C-C single bond and C-N bond, and the binding energy at 289.23 eV is attributable to π-π bond structure on PANI/PPy (Fig. 1d). The binding energy at 399.8 eV corresponds to the pyrrolic N (Fig. 1e). The peaks at 529.33 and 531.22 eV correspond to Cu-O bond and Fe-O bond, respectively (Fig. 1f).

The SEM images reveal that NIP-CuFeO$_2$@MnO$_2$ and MIP-CuFeO$_2$@MnO$_2$ are consisted of hierarchical and porous microspheres



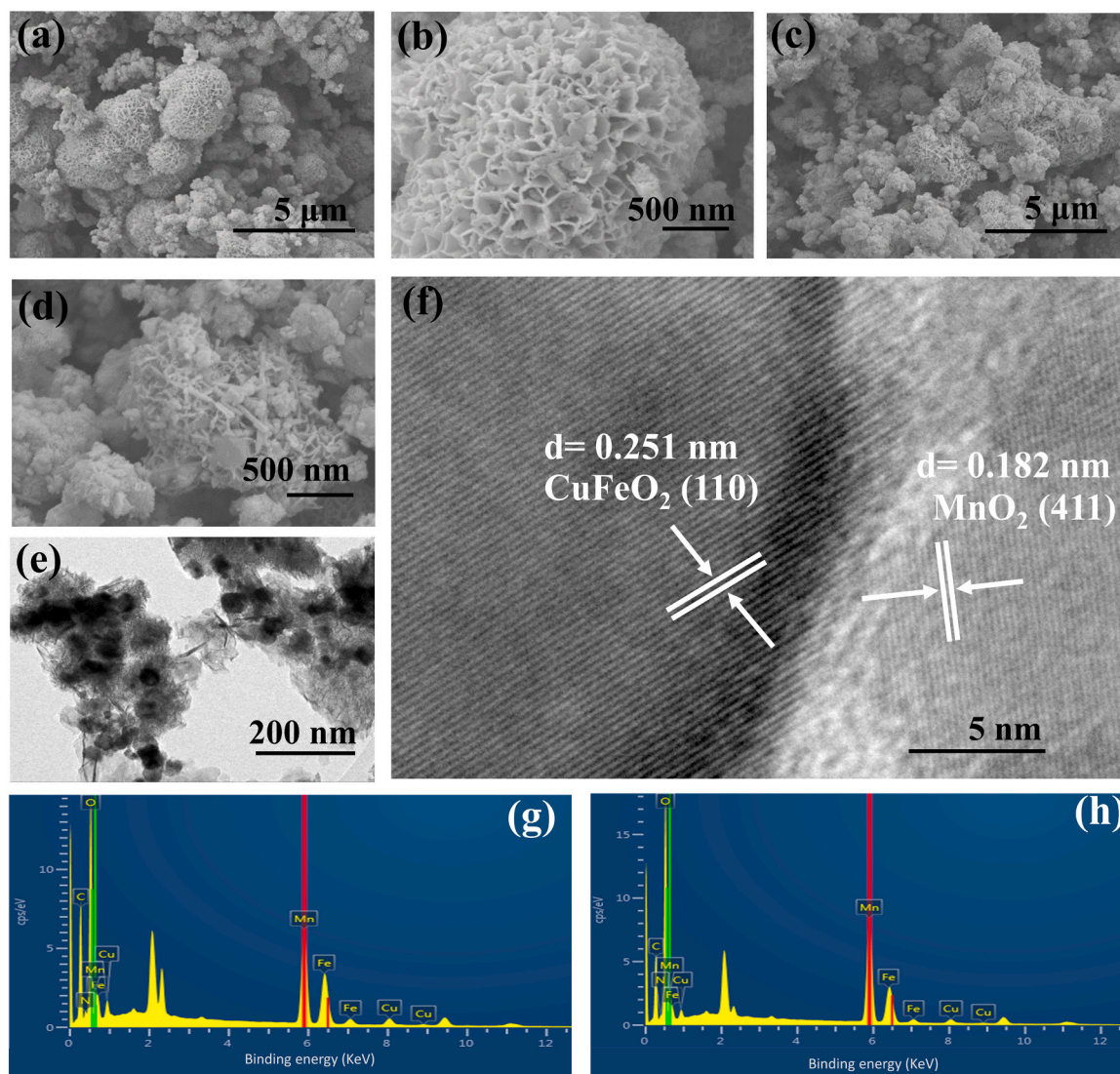**Fig. 2.** SEM images of MIP-CuFeO$_2$@MnO$_2$ (a, b) and NIP-CuFeO$_2$@MnO$_2$ (c, d); TEM (e) and HRTEM (f) images of MIP-CuFeO$_2$@MnO$_2$; EDX analysis of MIP-CuFeO$_2$@MnO$_2$ (g) and NIP-CuFeO$_2$@MnO$_2$ (h).

with different sizes in range of 0.5–2.5 μm, which are self-assembly of nanosheets. Moreover, more nanosheets are observed in MIP-CuFeO$_2$@MnO$_2$ (Fig. 2a-d). TEM confirms the core-shell structure of inorganic crystal/polymer layer (Fig. 2e). In the HRTEM image of MIP-CuFeO$_2$@MnO$_2$, the lattice fringes of 0.251 and 0.182 nm correspond to CuFeO$_2$ (110) and MnO$_2$ (411) crystal planes, respectively (Fig. 2f). In EDX spectra of (1:1) NIP-CuFeO$_2$@MnO$_2$ and MIP-CuFeO$_2$@MnO$_2$, Fe, Cu, Mn, C, O and N elements appear (Fig. 2g, h). HRTEM, along with XRD, EDX and TEM, confirms the successful synthesis of CuFeO$_2$@MnO$_2$ with group-imprinted layer.

The N$_2$ adsorption-desorption isotherms of CuFeO$_2$@MnO$_2$, NIP-CuFeO$_2$@MnO$_2$ and MIP-CuFeO$_2$@MnO$_2$ can be classified as type IV, and the hysteresis loop is H4 type (Fig. 3a), which suggests the presence of narrow slit-like pores generated by layered structures and narrow pore size distribution. Most of the pores are distributed in 2–30 nm (Fig. 3b), indicating that CuFeO$_2$@MnO$_2$, NIP-CuFeO$_2$@MnO$_2$ and MIP-CuFeO$_2$@MnO$_2$ are mesoporous materials. The specific surface areas of MIP-CuFeO$_2$@MnO$_2$, NIP-CuFeO$_2$@MnO$_2$ and CuFeO$_2$@MnO$_2$ are 134.03, 75.53 and 34.16 m$^2$/g, respectively (Table S2). MIP-CuFeO$_2$@MnO$_2$ is 3.92 times that of CuFeO$_2$@MnO$_2$ and 1.77 times that of NIP-CuFeO$_2$@MnO$_2$, which is probably due to many imprinted cavities in the organic copolymer layer of MIP-CuFeO$_2$@MnO$_2$ [41].

The magnetic hysteresis loops of CuFeO$_2$@MnO$_2$, NIP-CuFeO$_2$@MnO$_2$ and MIP-CuFeO$_2$@MnO$_2$ are shown in Fig. 3c. All the samples show superparamagnetic response. The saturation magnetization of CuFeO$_2$@MnO$_2$, NIP-CuFeO$_2$@MnO$_2$ and MIP-CuFeO$_2$@MnO$_2$ is 5.28, 5.79 and 5.33 emu/g, respectively (Table S3). Although the magnetic performance is relatively weak, these samples can be easily recovered from aqueous solution under external magnetic field.

### 3.2. Photogenerated charge separation and transfer

The photogenerated charge separation and transfer dynamics were characterized by photocurrent and electrochemical impedance spectra (EIS). In general, higher photocurrent intensity indicates higher separation efficiency of photogenerated charge carriers. CuFeO$_2$@MnO$_2$, MIP-CuFeO$_2$@MnO$_2$ and NIP-CuFeO$_2$@MnO$_2$ have photocurrent response, and the photocurrent intensity increases with the following order: CuFeO$_2$@MnO$_2$ < NIP-CuFeO$_2$@MnO$_2$ < MIP-CuFeO$_2$@MnO$_2$ (Fig. 4a). The obtained Nyquist plots consist of three arcs. The arc in the range of 0–25 Ω is attributed to the diffusion of ions into the pores of the electrode. The semicircle in the low-frequency portion is a line, which corresponds to Nernst bulk diffusion impedance. The semicircle in the middle-frequency portion of EIS can reflect the charge transfer resistance between the electrode surface and the reactants in the solution [42]. The small radius of EIS Nyquist semicircles indicates low interfacial resistance and efficient charge transport. The impedance arc radius of these photocatalysts increases as follows: MIP-CuFeO$_2$ @MnO$_2$ < NIP-CuFeO$_2$@MnO$_2$ ≈ CuFeO$_2$@MnO$_2$ (Fig. 4b). In about 25–125 Ω

region of EIS, the smaller semicircle radius of MIP-CuFeO$_2$ @MnO$_2$ than that of CuFeO$_2$@MnO$_2$ and CuFeO$_2$@MnO$_2$ suggests smaller charge transfer resistance at the electrode/electrolyte interface of MIP-CuFeO$_2$@MnO$_2$ during migration, leading to more highly-effective charge transport. The increased charge separation efficiency and smaller interfacial resistance of MIP-CuFeO$_2$@MnO$_2$ could be attributed to that more nanosheet and imprinted cavities shorten the distance of carrier migration, reduce the interfacial electron barrier, enhance light absorption, and strong interaction among CuFeO$_2$, MnO$_2$ and copolymer layer [43].

### 3.3. Adsorption kinetics, isotherm and recognition selectivity

The molar ratios of dummy template molecule to functional monomers (aniline and pyrrole) were optimized for synthesis of MIP-CuFeO$_2$@MnO$_2$, and the adsorption capacities for tetracycline of MIP-CuFeO$_2$@MnO$_2$ with different molar ratios of acrylamide to mixture of aniline and pyrrole ($n_{acrylamide}$: $n_{(aniline + pyrrole)}$ = 1:10, 1:6, 1:4, 1:2 and 1:1; $n_{aniline}$: $n_{pyrrole}$ = 1:1). The n$_{(aniline+pyrrole)}$ means the sum of the mole of aniline and the mole of pyrrole) were shown in Fig. 5a. With increasing $n_{acrylamide}$: $n_{(aniline + pyrrole)}$ from 1:10–1:4, more tetracycline would bind. MIP-CuFeO$_2$@MnO$_2$ (1:4) exhibited excellent binding performance for tetracycline. With the further increase of the molar ratio of $n_{acrylamide}$: $n_{(aniline + pyrrole)}$ from 1:4–1:1, there is no increase in the adsorption capacity of MIP-CuFeO$_2$@MnO$_2$ for TC. This phenomenon was attributed to that deficient content of functional monomer gave rise to insufficient selective binding sites and weak specific adsorption ability, while excessive functional monomers increased the content of residual non-assembled functional monomer in the pre-polymerization mixture, and the pre-assembly complex and selective binding sites did not increase. In the following experiments, the optimal raw material ratios for synthesis of MIP-CuFeO$_2$@MnO$_2$ are listed as follows: $n_{acrylamide}$: $n_{(aniline + pyrrole)}$ = 1:4, $n_{aniline}$: $n_{pyrrole}$ = 1:1.

The adsorption kinetics of tetracycline on NIP-CuFeO$_2$@MnO$_2$ and MIP-CuFeO$_2$@MnO$_2$ are presented in Fig. 5b. The adsorption rate of tetracycline on MIP-CuFeO$_2$@MnO$_2$ is faster than that of NIP-CuFeO$_2$@MnO$_2$ due to more imprinted cavities of MIP-CuFeO$_2$@MnO$_2$. The adsorption amount of tetracycline on NIP-CuFeO$_2$@MnO$_2$ and MIP-CuFeO$_2$@MnO$_2$ increased rapidly in first 10 min, then the adsorption rate decreases with time, and it takes 22 min to reach adsorption equilibrium. The dynamic adsorption process of tetracycline on MIP-CuFeO$_2$@MnO$_2$ and NIP-CuFeO$_2$@MnO$_2$ were fitted by pseudo-first-order and pseudo-second-order model (Text S4). The rate constant (k$_1$) of pseudo-first-order model was obtained from the slope of "ln (Q$_e$ - Q$_t$) versus t'' curves (Fig. S2). The rate constant (k$_2$) of pseudo-second-order model and the amount of adsorbed tetracycline at equilibrium (Q$_e$) can be acquired from the slope and intercept of the t/Q$_t$ versus t curves, respectively (Fig. 5c). The k$_1$, k$_2$, correlation coefficients (R$^2$) and other parameters was listed in Table S4. Compared with the data
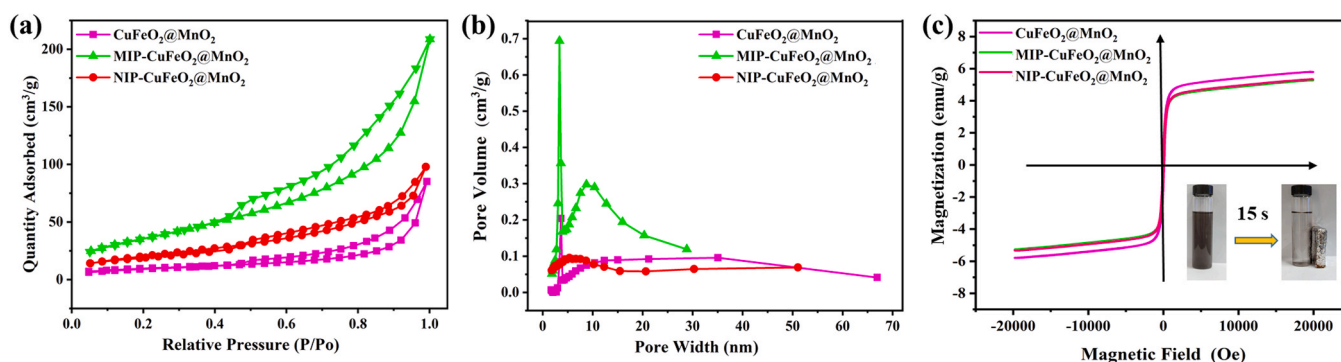


**Fig. 3.** (a) N$_2$ adsorption-desorption isotherms, (b) pore-size distribution curves and (c) magnetic hysteresis loops for CuFeO$_2$@MnO$_2$, MIP-CuFeO$_2$@MnO$_2$, and NIP-CuFeO$_2$@MnO$_2$.
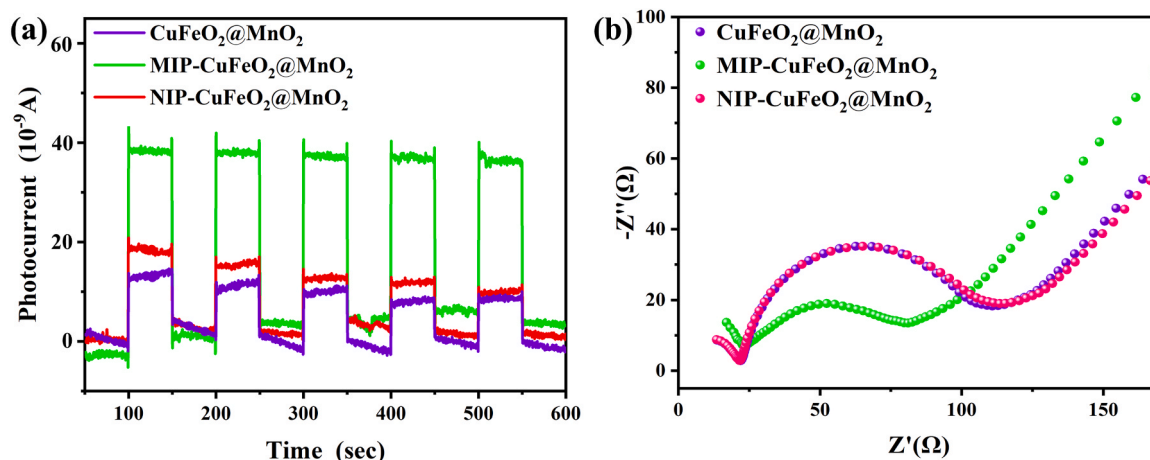
**Fig. 4.** (a) Photocurrent and (b) EIS of $CuFeO_2@MnO_2$, $NIP-CuFeO_2@MnO_2$ and $MIP-CuFeO_2@MnO_2$.
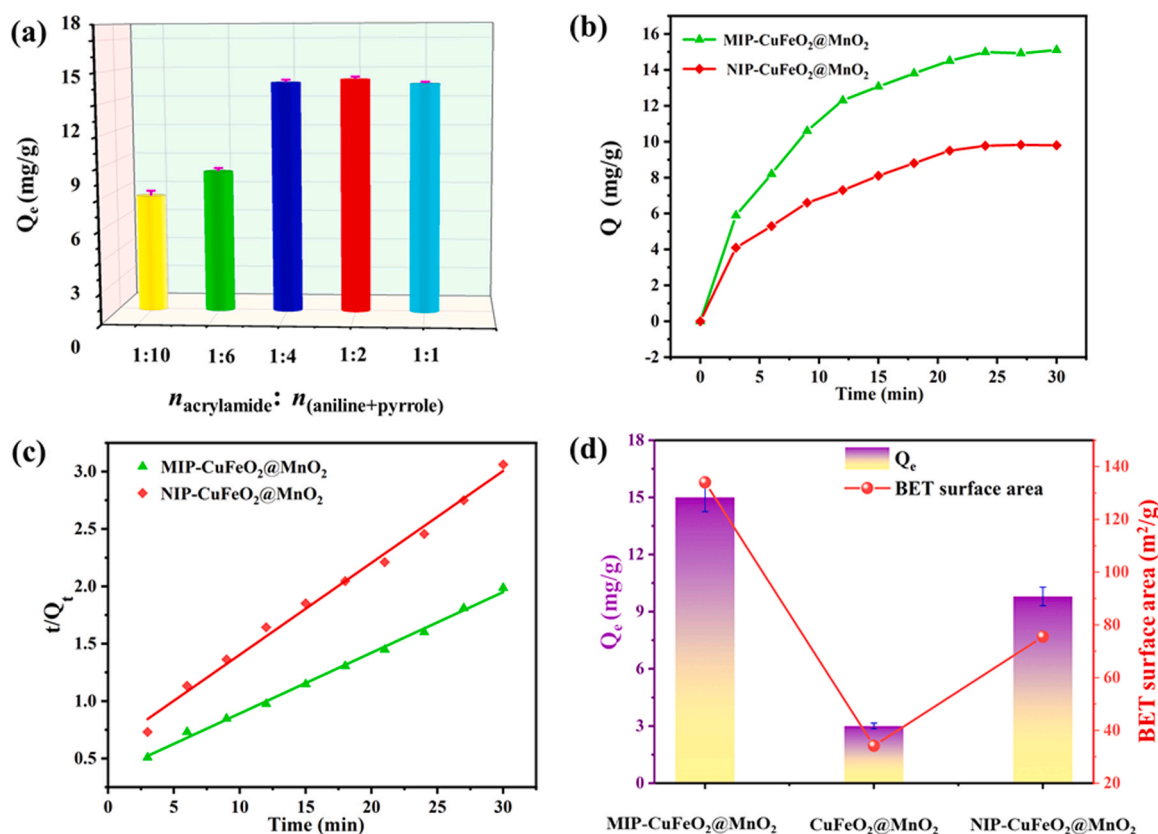


**Fig. 5.** (a) Adsorption capacity of $MIP-CuFeO_2@MnO_2$ with different ratio of template molecule to functional monomer; (b) Adsorption kinetics of TC on $MIP-CuFeO_2@MnO_2$ and $NIP-CuFeO_2@MnO_2$ and fitting curves; (c) The fitting curves of pseudo-second-order model; (d) The correlation between specific surface area and adsorption performance.

obtained from pseudo first-order model, the calculated equilibrium adsorption capacities of $MIP-CuFeO_2@MnO_2$ ($Q_{e,cal}$= 15.43 mg/g) and $NIP-CuFeO_2@MnO_2$ ($Q_{e,cal}$= 10.04 mg/g) from pseudo-second-order kinetic model are closer to the experimental values ($Q_{e,exp}$= 15.2 mg/g for $MIP-CuFeO_2@MnO_2$, $Q_{e,exp}$= 9.8 mg/g for $NIP-CuFeO_2@MnO_2$) with higher $R^2$ values, suggesting that the adsorption of tetracycline on $NIP-CuFeO_2@MnO_2$ and $MIP-CuFeO_2@MnO_2$ is in line with the pseudo-second-order model. The pseudo-second-order model is based on the assumption that the adsorption rate is controlled by the chemical adsorption mechanism, which involves electron sharing or electron transfer between the adsorbate and adsorbent. Thus, the adsorption

process of tetracycline on $NIP-CuFeO_2@MnO_2$ and $MIP-CuFeO_2@MnO_2$ was dominated by chemisorption [44]. The correlation between the adsorption capacity and its specific surface area was explored (Fig. 5d). The positive correlation of adsorption capacity with the specific surface area indicates that the vital role of imprinted cavities in the organic copolymer layer of $MIP-CuFeO_2@MnO_2$ in adsorption process.

Fig. 6 shows the adsorption isotherms of tetracycline on $NIP-CuFeO_2@MnO_2$ and $MIP-CuFeO_2@MnO_2$. The adsorption capacity of $NIP-CuFeO_2@MnO_2$ and $MIP-CuFeO_2@MnO_2$ increases with increasing initial TC concentration, and the adsorption capacity of $NIP-CuFeO_2@MnO_2$ and $MIP-CuFeO_2@MnO_2$ keeps unchanged if initial TC
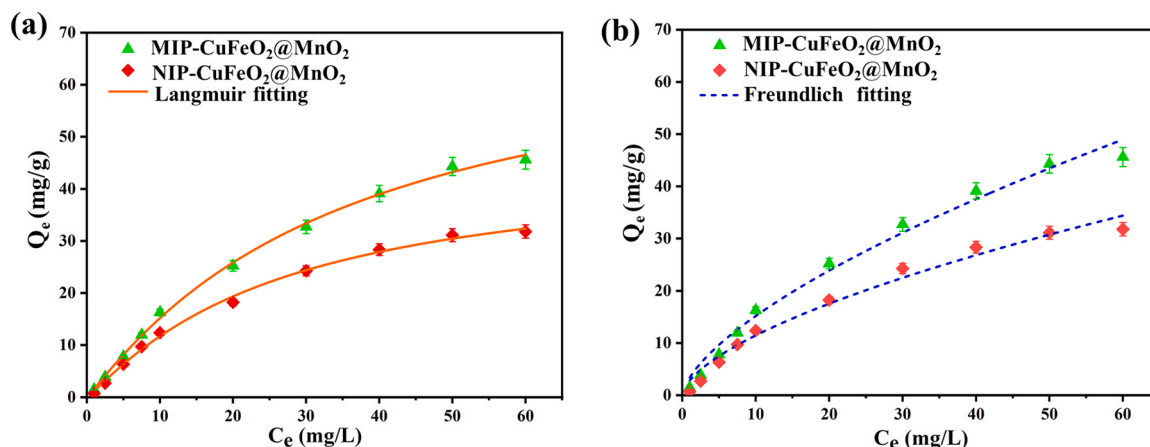
**Fig. 6.** Adsorption isotherms of TC on MIP-CuFeO$_2$@MnO$_2$ and NIP-CuFeO$_2$@MnO$_2$.

concentration > 50 mg/L. The adsorption capacity of MIP-CuFeO$_2$@MnO$_2$ is higher than that of NIP-CuFeO$_2$@MnO$_2$. The adsorption isothermal data was fitted with Langmuir and Freundlich model [45], and the fitting parameters were listed in Table S5. The higher correlation coefficient (R$^2$ =0.997) obtained by Langmuir model than that by Freundlich model indicates monolayer surface adsorption of tetracycline on NIP-CuFeO$_2$@MnO$_2$ and MIP-CuFeO$_2$@MnO$_2$. In addition, the theoretical maximum adsorption capacity (Q$_{max}$) of MIP-CuFeO$_2$@MnO$_2$ fitted by the Langmuir model is as high as 45.6 mg/g, which is 1.44 folds larger than that of NIP-CuFeO$_2$@MnO$_2$, indicating that the imprinted cavities are beneficial for TC adsorption.

The adsorption selectivity of photocatalyst towards organic pollutants in wastewater is essential for toxicity reduction. To evaluate the adsorption selectivity of NIP-CuFeO$_2$@MnO$_2$ and MIP-CuFeO$_2$@MnO$_2$, the structural analog of TC represented by IBP was selected as competitors for the competitive adsorption of TC because ibuprofen has the same benzene ring, methyl group, carbon-oxygen single and double bond as TC (Fig. S3). As shown in Fig. 7, MIP-CuFeO$_2$@MnO$_2$ has a stronger binding capacity for TC than IBP in single and binary solution. In binary solution of ibuprofen and TC, the distribution coefficient ($k_d$) value of MIP-CuFeO$_2$@MnO$_2$ for TC was 0.308 L/g, which is 6.86 times

more than for the IBP (only 0.045 L/g). The selection factor ($\alpha$) of MIP-CuFeO$_2$@MnO$_2$ is about 3.2 times that of NIP-CuFeO$_2$@MnO$_2$ (Table 1), indicating that the imprinted cavities of MIP-CuFeO$_2$@MnO$_2$ which matched with the amide groups of TC can selectively recognize and adsorb TC.

### 3.4. The preferential degradation performance of MIP-CuFeO$_2$@MnO$_2$

The visible-light photocatalytic activities of CuFeO$_2$@MnO$_2$, NIP-CuFeO$_2$@MnO$_2$ and MIP-CuFeO$_2$@MnO$_2$ were investigated by

**Table 1**
Selectivity and distribution coefficient of MIP-CuFeO$_2$@MnO$_2$ and NIP-CuFeO$_2$@MnO$_2$ for TC.

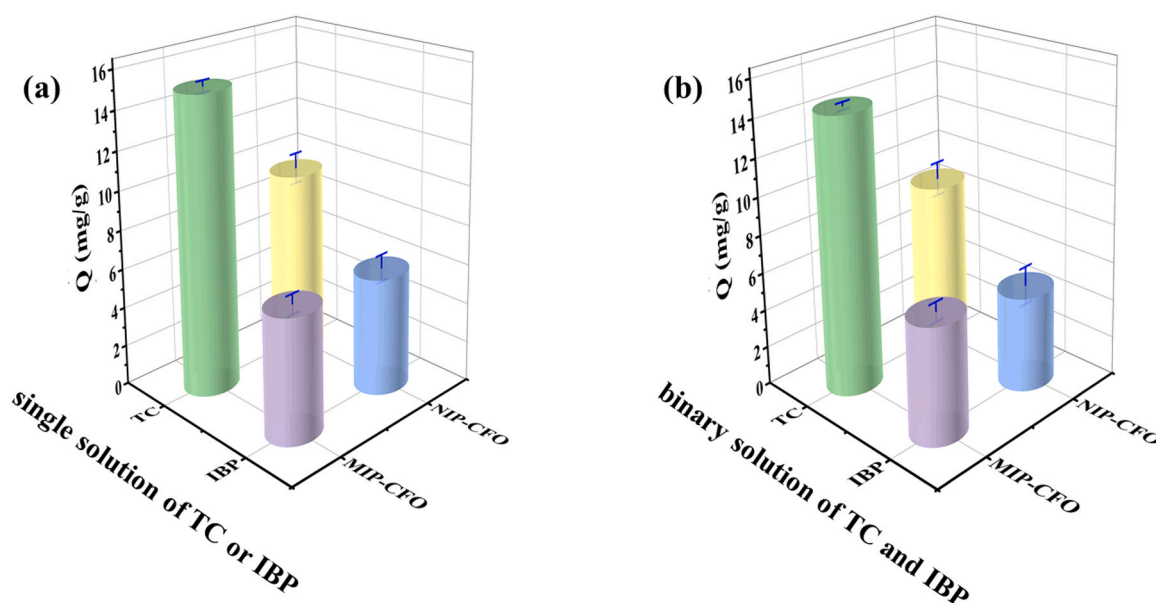| Imprinting parameters | MIP-CuFeO$_2$@MnO$_2$ | | NIP-CuFeO$_2$@MnO$_2$ | |
|---|---|---|---|---|
| | TC | IBP | TC | IBP |
| $Q_e$ (mg) | 0.755 | 0.310 | 0.475 | 0.295 |
| $C_e$ (mg/L) | 2.45 | 6.90 | 5.25 | 7.05 |
| $K_d$ (L/g) | 0.308 | 0.045 | 0.091 | 0.042 |
| $\alpha$ | 6.86 | | 2.17 | |



**Fig. 7.** Adsorption amounts of TC and IBP by MIP-CuFeO$_2$@MnO$_2$ and NIP-CuFeO$_2$@MnO$_2$ in (a) single-component solution, and (b) binary mixture solution of TC and IBP.

degrading TC aqueous solution (Fig. 8a). As shown in Fig. 8b, adsorption makes a great contribution to the TC removal. After adsorption equilibrium, the TC concentration in presence of $CuFeO_2@MnO_2$, NIP-$CuFeO_2@MnO_2$ and MIP-$CuFeO_2@MnO_2$ deceased by about 17%, 49% and 75.5%, respectively. The mass transfer process has vital effect on the subsequent photocatalytic degradation. After 100 min photocatalysis, tetracycline removal efficiency by $CuFeO_2@MnO_2$, NIP-$CuFeO_2@MnO_2$ and MIP-$CuFeO_2@MnO_2$ is 52%, 77% and 93%, respectively. The advantages of MIP-$CuFeO_2@MnO_2$ over $CuFeO_2@MnO_2$ and NIP-$CuFeO_2@MnO_2$ in degradation efficiency and speed could be attributable to more active sites and imprinted cavities which can quickly recognize and adsorb TC molecules. To verify the feasibility of MIP-$CuFeO_2@MnO_2$ under natural light, the photocatalytic degradation of TC under visible light and sunlight (at noon of July 12, 2023, Nanchang) was compared (Fig. S4), the degradation efficiency of TC by MIP-$CuFeO_2@MnO_2$ under visible light is similar to that under sunlight, indicating that MIP-$CuFeO_2@MnO_2$ is effective under visible light and sunlight.

The total organic carbon (TOC) and ammonium ion ($NH_4^+$) concentration in the TC degradation solution were also determined to assess the mineralization degree of organic pollutants in the solution (Fig. 8c and d). After 11 h photocatalysis, the TOC removal rate of TC solution was 41.98%, and $NH_4^+$ concentration increased from 0 to 1.16 mg/L, suggesting that TC molecules can be mineralized into $CO_2$, $H_2O$ and $NH_4^+$ ions. Moreover, the stability of MIP-$CuFeO_2@MnO_2$ was investigated by repeated use in degrading tetracycline, FT-IR comparison between fresh and recovered MIP-$CuFeO_2@MnO_2$, and release of metal ions in reaction solution (Fig. S5). There is a slight decrease of TC degradation efficiency

after several cycles (Fig. S5a). Compared with the FT-IR spectra of fresh MIP-$CuFeO_2@MnO_2$, there is no obvious change of peak position except for slight shift of peaks at 3000–3600 $cm^{-1}$ and around 1250–1750 $cm^{-1}$ (Fig. S5b). The slight peak shift indicates the important role of hydrogen bond, and the bonding between C-N of MIP-$CuFeO_2@MnO_2$ and the hydroxyl groups of TC in the photocatalysis process. After photocatalytic reaction, the concentrations of $Cu^{2+}$, $Fe^{3+}$ and $Mn^{2+}$ ions in the reaction solution were 0.0257, 0.0101, and 0.0119 mg/L, respectively. The concentrations of $Cu^{2+}$, $Fe^{3+}$ and $Mn^{2+}$ ions were very low, further confirming that MIP-$CuFeO_2@MnO_2$ photocatalyst is relatively stable (Fig. S5c). Compared with the SEM of fresh MIP-$CuFeO_2@MnO_2$, the morphology of the recovered MIP-$CuFeO_2@MnO_2$ did not change obviously after several cycles (Fig. S6), further confirming the stable microstructure.

To explore the main reactive species in the TC photodegradation by MIP-$CuFeO_2@MnO_2$, isopropanol (IPA), triethanolamine (TEOA), and p-benzoquinone (BQ) were added to trap hydroxyl radicals ($^\bullet OH$), $h^+$ and superoxide radicals ($O_2^-$). The degradation efficiency of tetracycline is decreased from 92% to 62.5%, 54.38% and 78.9% in presence of IPA, TEOA and BQ, respectively (Fig. 9a). The above trapping experiment indicated that $h^+$, $^\bullet OH$ and $O_2^{\bullet-}$ are jointly involved in TC degradation (Fig. 9b, c and d). The active species were confirmed by electron spin resonance (ESR) with 5,5-dimethyl-1-pyrroline N-oxide (DMPO) and 2, 2, 6, 6-tetramethylpiperidinooxy (TEMPO). DMPO can capture $O_2^{\bullet-}$ and $^\bullet OH$ radicals to generate the long-lived DMPO-$O_2^{\bullet-}$ and DMPO-$^\bullet OH$ adducts, while TEMPO can capture photogenerated $e^-$ and $h^+$ [46]. The peak intensity of TEMPO-$h^+$ is the highest in the dark, but becomes weaker with the extension of exposure time, which is accordant with the



**Fig. 8.** (a) Tetracycline removal by adsorption and photocatalysis of $CuFeO_2@MnO_2$, NIP-$CuFeO_2@MnO_2$ and MIP-$CuFeO_2@MnO_2$; (b) The correlation between specific surface area and photocatalytic performance; (c) TOC change of tetracycline solution by photocatalysis of MIP-$CuFeO_2@MnO_2$; (d) Concentration change of $NH_4^+$ ions in tetracycline solution by photocatalysis of MIP-$CuFeO_2@MnO_2$.

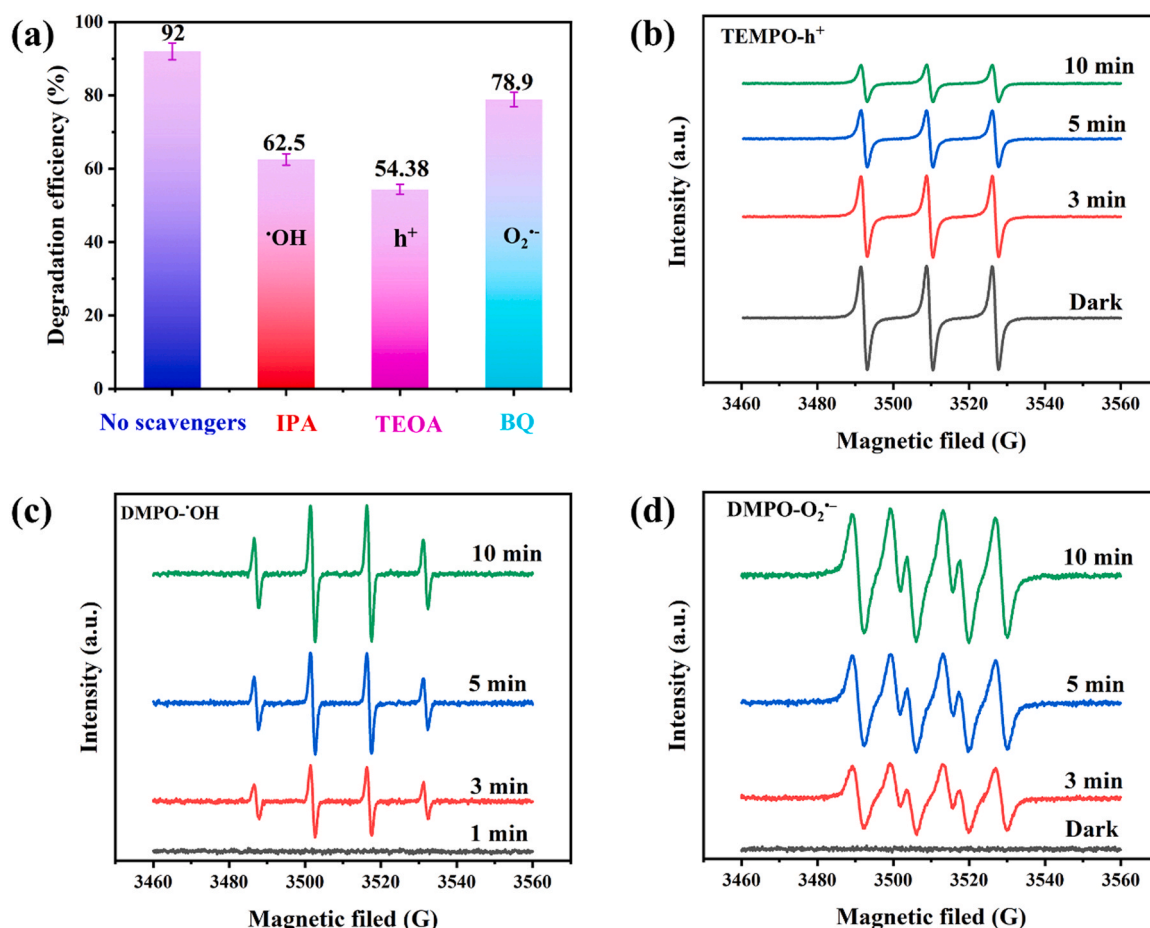**Fig. 9.** (a) Trapping experiments for active species; ESR of DMPO-h$^+$ (b), DMPO-$^{\bullet}$OH (c) and DMPO-O$_2^{\bullet-}$ (d).

reported results (Fig. 9b). No DMPO-$^{\bullet}$OH and DMPO-O$_2^{\bullet-}$ peaks were observed in the dark, and the intensity of DMPO-$^{\bullet}$OH and DMPO-O$_2^{\bullet-}$ peaks enhanced with extending exposure time of visible light (Fig. 9c and d).

In order to further investigate the role of the footprint cavities in target degradation of toxic chemical groups, the UV–visible full-scan spectra of tetracycline solution during the photocatalytic process was monitored (Fig. S7). The characteristic absorption peaks of tetracycline are located at 274 and 367 nm. The absorption peak at 274 nm is ascribed to aromatic ring A and the amide group, while absorption peak at 367 nm is related with the aromatic ring C and D comprising the extended chromophores. Compared with NIP-CuFeO$_2$@MnO$_2$, there is more obvious attenuation in the absorption peak of tetracycline at 274 nm during the photocatalysis process of MIP-CuFeO$_2$@MnO$_2$, indicating the preferential destruction of aromatic ring A and the amide groups [47]. According to the reported literature, the absorption peak at 367 nm is more easily disappeared, which was not observed in photocatalysis of MIP-CuFeO$_2$@MnO$_2$. In the photocatalysis of NIP-CuFeO$_2$@MnO$_2$, there is more obvious red-shift of absorption peak at 367 nm, indicating the destruction of aromatic ring C and D.

The active sites on TC were studied by density function theory (DFT) calculation, and then the degradation path in the photocatalytic system was demonstrated. The molecular structure model of TC and the calculation results of Fukui function are shown in Fig. 10. The f$^-$, f$^+$ and f$^0$ are used to investigate electrophilic reaction, nucleophilic reaction and free radical reaction, respectively. The green color of C1 and C5 connected to the amide group, the O23 of C═O bond and O55 of C═O corresponded to the active sites for electrophilic reaction (Fig. 10b). The green color of O25 in ketone group indicates that this site was vulnerable

to the attack of free radicals. It is worth noting that the two ring structures connected by C14 and C15 is almost colorless, indicating that these sites have low reaction reactivity (Fig. 10c and d). According to previous studies, the involvement of O$_2^{\bullet-}$ is usually considered as a free radical reaction, while $^{\bullet}$OH can be regarded as electrophilic groups. As shown in Table 2, the positive f$^-$ values decreased as follows: O23 >C5 >C1 >O55 >O42 >C18 >N43, further indicating O23, C5, C1 and O55 are more vulnerable to electrophilic reactions. Although the f$^-$ value of N43 is lower than that of O23, C5, C1 and O55, the easy degradation of N43 in experiment also illustrated the high photocatalytic selectivity. The O25 with f$^+$ value of 0.0929 and f$^0$ value of 0.1401 also confirmed that O25 is prone to be attacked by free radicals (Table 2).

To further explore the different degradation paths of TC by MIP-CuFeO$_2$@MnO$_2$ and NIP-CuFeO$_2$@MnO$_2$, the degradation intermediates of TC during the photocatalytic process were analyzed by HPLC-MS (Fig. 11). The retention time of degradation products was shown in Fig. S8. The difference of retention time indicates different intermediate products. The peak of TC appears at $m/z$ of 445.0. As the degradation going on, several peaks at 428.0, 415.0, 340.0, 274.0 and 157.9 corresponding to intermediate products appear in presence of MIP-CuFeO$_2$@MnO$_2$. In presence of NIP-CuFeO$_2$@MnO$_2$, the $m/z$ peaks of degradation intermediate products appeared at 415, 318, 223, 165, and 157.9. According to the $m/z$ peaks of degradation intermediates, the degradation pathways of tetracycline by visible-light photocatalysis of MIP-CuFeO$_2$@MnO$_2$ (I) and NIP-CuFeO$_2$@MnO$_2$ (II) were inferred (Fig. 11). In presence of MIP-CuFeO$_2$@MnO$_2$, the amide groups were preferentially attacked and destructed to produce intermediate product, then M1 was formed via demethylation. The demethylation and
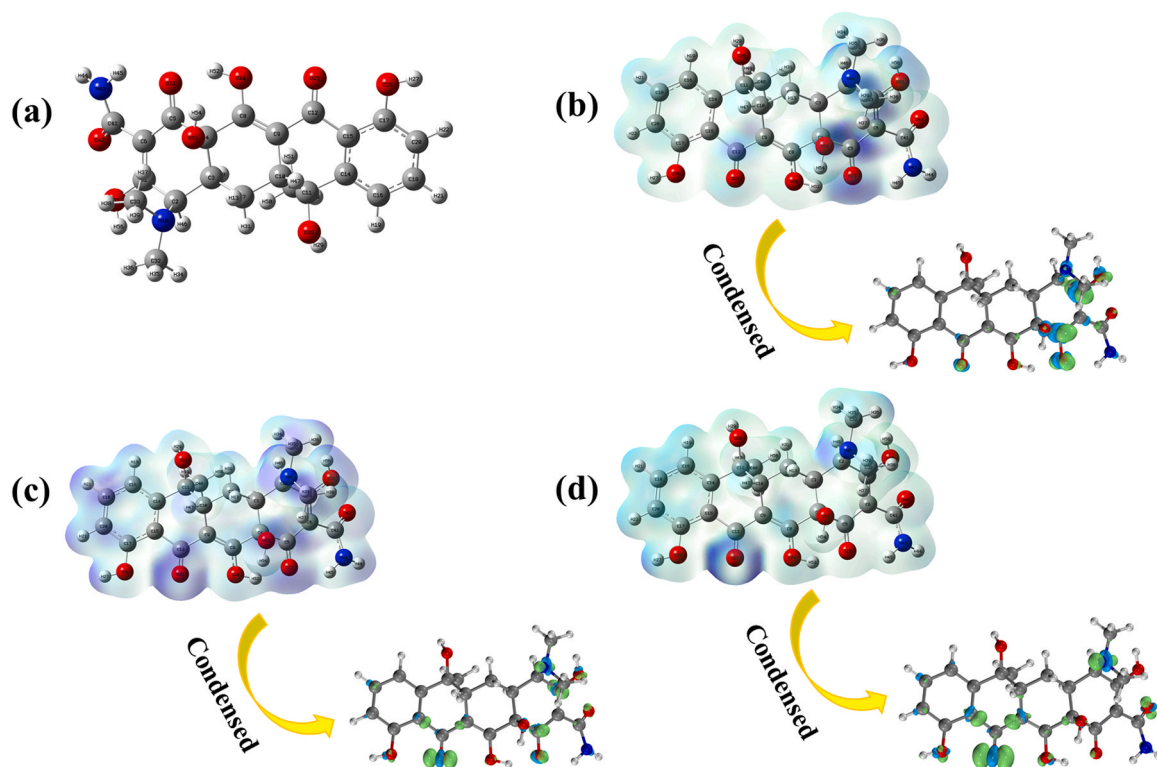
**Fig. 10.** (a) The optimized molecular model of TC; The Fukui function mapped electron density isosurface and atomic coloring maps of condensed Fukui function: (b) f, (c) $f^+$, and (d) $f^0$ (The dark blue on the isosurface corresponds to the larger positive value of the Fukui function, and green and blue corresponds to positive and negative value, respectively.).

**Table 2**
Condensed Fukui function for TC.

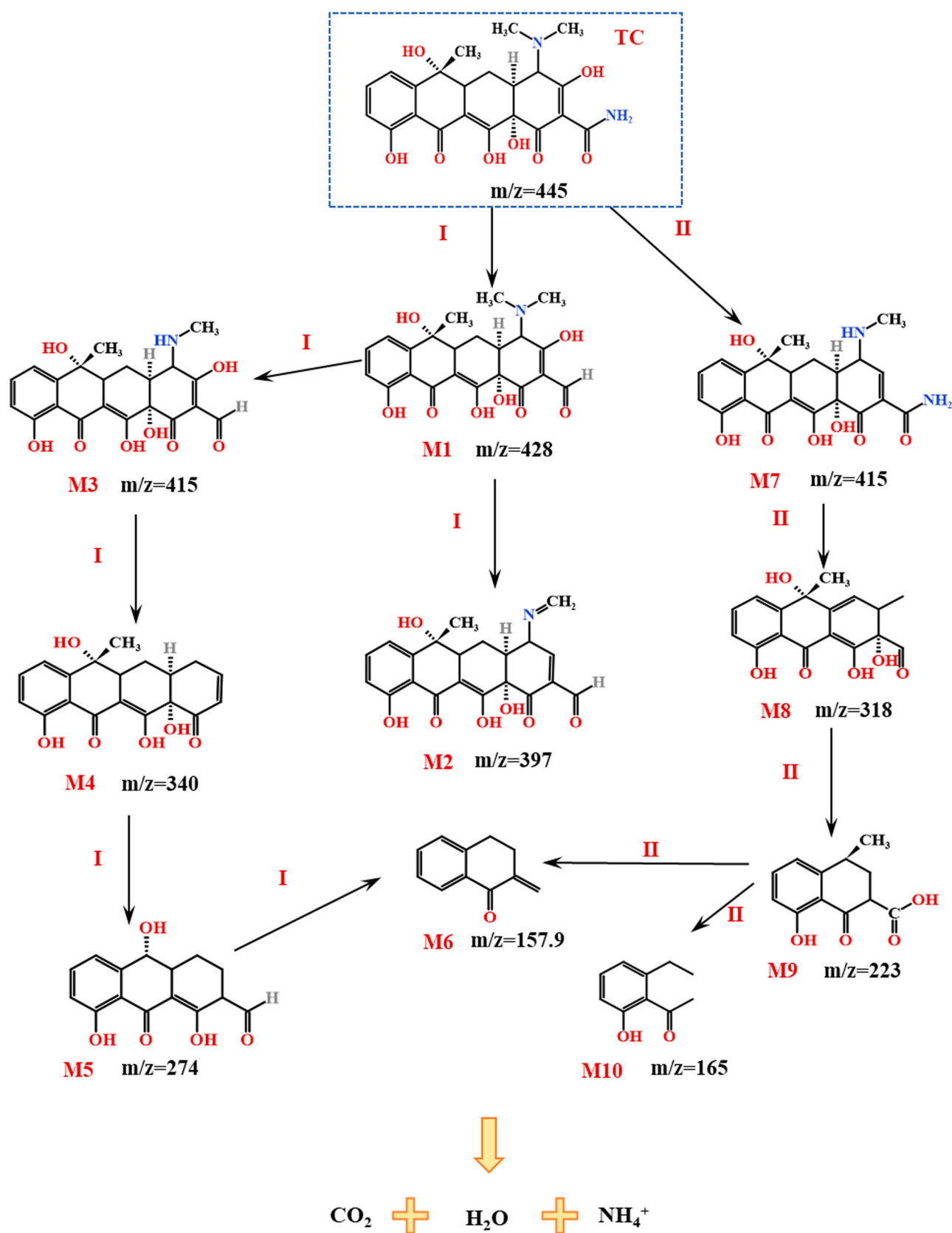| Atom | q (N) | q (N + 1) | q (N-1) | f | $f^+$ | $f^0$ | CDD |
|---|---|---|---|---|---|---|---|
| 1(C) | 0.1263 | 0.0384 | 0.1333 | 0.0879 | 0.0475 | 0.007 | 0.0809 |
| 2(C) | 0.024 | 0.0164 | 0.0308 | 0.0077 | 0.0072 | 0.0068 | 0.0009 |
| 3(C) | -0.027 | -0.0282 | -0.0233 | 0.0012 | 0.0024 | 0.0037 | -0.0026 |
| 4(C) | 0.0685 | 0.0586 | 0.0757 | 0.0100 | 0.0086 | 0.0072 | 0.0028 |
| 5(C) | 0.1393 | 0.051 | 0.1435 | 0.0883 | 0.0463 | 0.0042 | 0.0841 |
| 6(C) | -0.0577 | -0.0865 | -0.0467 | 0.0288 | 0.0199 | 0.011 | 0.0178 |
| 7(C) | -0.0574 | -0.0636 | -0.0498 | 0.0062 | 0.0069 | 0.0076 | -0.0015 |
| 8(C) | 0.0771 | 0.0689 | 0.1023 | 0.0083 | 0.0167 | 0.0252 | -0.0169 |
| 9(C) | -0.052 | -0.0723 | -0.0302 | 0.0203 | 0.0210 | 0.0218 | -0.0015 |
| 10(C) | -0.0202 | -0.0238 | -0.0141 | 0.0035 | 0.0049 | 0.0062 | -0.0026 |
| 11(C) | 0.0845 | 0.0837 | 0.0854 | 0.0008 | 0.0009 | 0.0009 | -0.0001 |
| 12(C) | 0.1242 | 0.0937 | 0.1618 | 0.0305 | 0.0340 | 0.0376 | -0.0071 |
| 14(C) | -0.0005 | -0.0075 | 0.0142 | 0.0070 | 0.0108 | 0.0147 | -0.0077 |
| 15(C) | -0.0344 | -0.0377 | -0.021 | 0.0033 | 0.0084 | 0.0134 | -0.010 |
| 16(C) | -0.0668 | -0.0793 | -0.036 | 0.0125 | 0.0216 | 0.0308 | -0.0184 |
| 17(C) | 0.0873 | 0.0741 | 0.1051 | 0.0131 | 0.0155 | 0.0179 | -0.0048 |
| 18(C) | -0.0346 | -0.065 | -0.0013 | 0.0304 | 0.0319 | 0.0333 | -0.0029 |
| 20(C) | -0.0748 | -0.0944 | -0.0455 | 0.0197 | 0.0245 | 0.0293 | -0.0096 |
| 23(O) | -0.2104 | -0.3017 | -0.1915 | 0.0912 | 0.0551 | 0.019 | 0.0723 |
| 24(O) | -0.1762 | -0.1949 | -0.1439 | 0.0187 | 0.0255 | 0.0323 | -0.0136 |
| 25(O) | -0.2439 | -0.2895 | -0.1038 | 0.0457 | 0.0929 | 0.1401 | -0.0944 |
| 26(O) | -0.1664 | -0.177 | -0.1386 | 0.0106 | 0.0192 | 0.0278 | -0.0173 |
| 28(O) | -0.2138 | -0.2205 | -0.2032 | 0.0067 | 0.0086 | 0.0106 | -0.0039 |
| 32(C) | -0.0395 | -0.0486 | -0.0267 | 0.0091 | 0.0110 | 0.0128 | -0.0037 |
| 33(C) | -0.0542 | -0.0593 | -0.0424 | 0.0051 | 0.0085 | 0.0119 | -0.0067 |
| 40(N) | -0.0808 | -0.0884 | -0.0349 | 0.0076 | 0.0267 | 0.0459 | -0.0383 |
| 41(C) | 0.1545 | 0.1468 | 0.1665 | 0.0078 | 0.0099 | 0.0119 | -0.0042 |
| 42(O) | -0.3056 | -0.3396 | -0.2587 | 0.0339 | 0.0404 | 0.0469 | -0.0130 |
| 43(N) | -0.1578 | -0.1763 | -0.1375 | 0.0186 | 0.0194 | 0.0203 | -0.0017 |
| 48(C) | -0.0961 | -0.0985 | -0.0922 | 0.0024 | 0.0031 | 0.0039 | -0.0014 |
| 53(O) | -0.1884 | -0.2141 | -0.1712 | 0.0257 | 0.0215 | 0.0172 | 0.0085 |
| 55(O) | -0.1259 | -0.1839 | -0.1086 | 0.0580 | 0.0377 | 0.0174 | 0.0406 |

**Fig. 11.** Possible degradation pathways of TC by photocatalysis of MIP-CuFeO$_2$@MnO$_2$ (I) and NIP-CuFeO$_2$@MnO$_2$ (II).

dehydroxylation leads to the production of M2 and M3. Deamination and dehydroxylation of M3 leads to the production of M4. M4 underwent demethylation and ring opening reaction to produce M5 and M6, and the intermediates were finally further mineralized to $CO_2$, $H_2O$ and $NH_4^+$. The degradation pathways of tetracycline by photocatalysis of NIP-CuFeO$_2$@MnO$_2$ is different from that by MIP-CuFeO$_2$@MnO$_2$. In presence of NIP-CuFeO$_2$@MnO$_2$, M8 was formed via demethylation of tetracycline. The demethylation and dehydroxylation leads to the production of M8 from M7, then M6 and M10 were generated through dehydroxylation, ring cleavage and dealkylation. The degradation pathways of tetracycline in presence of MIP-CuFeO$_2$@MnO$_2$ further illustrated the important role of footprint cavities in preferential destruction of toxic chemical groups.

### 3.5. Biological toxicity of intermediate products

The biotoxicity of TC and its degradation intermediates during the photocatalysis of MIP-CuFeO$_2$@MnO$_2$ was evaluated by the growth of *E. coli* in liquid medium containing TC and degradation solution (Fig. 12). The growth of *E. coli* in blank control and the liquid medium containing TC degradation solution undergoes three stages: lag phase (0–4 h), logarithmic phase (4–14 h) and stationary phase (14–24 h). Compared with the blank control, the growth of *E. coli* in liquid medium containing TC solution was severely inhibited, suggesting that high biological toxicity of TC, and its toxic chemical groups have strong inhibitory effect on *E. coli* growth. With the degradation going on, the *E. coli* grew more rapidly, and the *E. coli* growth in liquid medium containing degradation solution sampled after 60 min photocatalysis can be comparable to the blank control (Fig. 12a), indicating the rapid toxicity reduction of TC by photocatalysis of MIP-CuFeO$_2$@MnO$_2$. The *E. coli* after 25 h culture was visually observed. The liquid culture medium with adding TC solution is very clear, indicating that *E. coli* almost does not survive in presence of TC. In case of blank control and adding degradation solution to the liquid culture medium, the liquid culture medium becomes turbid to varying degrees due to the rapid propagation of *E. coli* (Fig. 12b). The visual observation also confirmed that photocatalysis of MIP-CuFeO$_2$@MnO$_2$ can rapidly reduce the eco-toxicity of TC. The acute and chronic toxicity of TC and its degradation intermediates were also analyzed by ECOSAR (Table S6). It can be seen from Table S6 that the toxicity of degradation intermediates is much lower than that of TC, indicating that the toxicity of tetracycline has been greatly reduced during the photocatalytic process, which is consistent with the results of *E. coli* growth in liquid medium containing degradation solution.
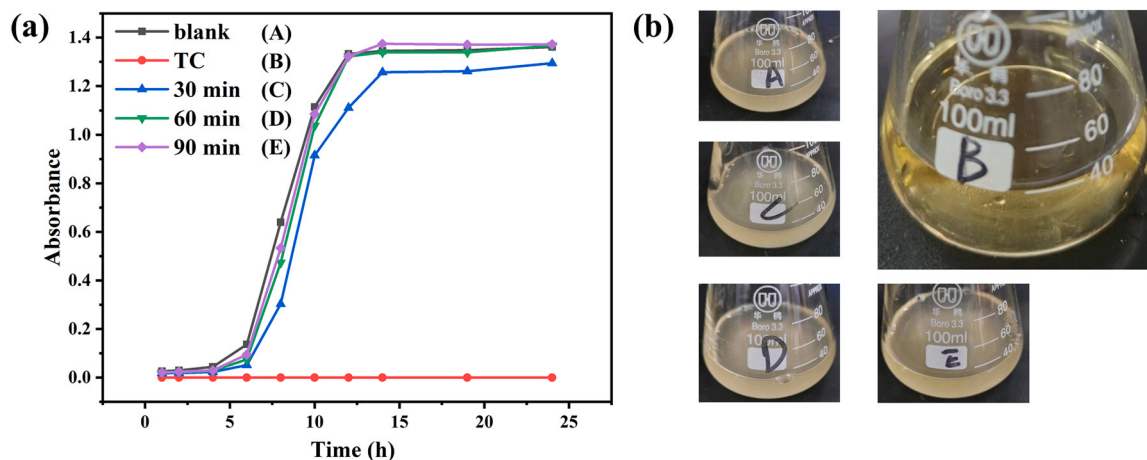
### 3.6. Preferential degradation mechanism of MIP-CuFeO$_2$@MnO$_2$

The recognition selectivity of MIP-CuFeO$_2$@MnO$_2$ for the amide group of tetracycline was also analyzed by DFT calculations. Based on hydrogen bonding theory, MIP-CuFeO$_2$@MnO$_2$ has high affinity for tetracycline via the hydrogen bonding between the -NH- sites (A and B) of PANI/PPy copolymers and six different sites of tetracycline (Fig. 13). To further figure out the binding sites between the PANI/PPy copolymers of MIP-CuFeO$_2$@MnO$_2$ and tetracycline, various possible models of tetracycline adsorption on MIP-CuFeO$_2$@MnO$_2$ were established to obtain interaction energy ($E_{int}$) via DFT calculation. As shown in Fig. 13, the $E_{int}$ of B-4 model is - 49.60 kcal/mol, which was the lowest among all the models, indicating that the hydrogen bonding between the amide groups of tetracycline at site 4 and -NH- at site B was the most favorable for the binding of tetracycline on MIP-CuFeO$_2$@MnO$_2$ under the same external condition, and amide groups of tetracycline can be preferentially bound on MIP-CuFeO$_2$@MnO$_2$. Moreover, the hydroxyl sites at site 1, 2 and 6 on tetracycline also have strong binding energy with -NH- at site A on PANI/PPy copolymer of MIP-CuFeO$_2$@MnO$_2$, and the carbonyl groups at site 3 and 5 also have strong binding energy with the site B of PANI/PPy, indicating that hydroxyl and carbonyl groups are also easily bound and degraded during the photocatalytic process.

FT-IR spectroscopy was utilized to further determine the specific adsorption and preferential degradation of amide groups (Fig. 14a). After adsorption, a new peak of N-H stretching vibration at 3735 cm$^{-1}$ appeared, indicating the adsorption of amide groups on MIP-CuFeO$_2$@MnO$_2$. After the photocatalytic process, this peak disappeared, indicating the preferential degradation of amide groups adsorbed on MIP-CuFeO$_2$@MnO$_2$ during the photocatalytic process. Moreover, the slight shift of wide peak at 3000–3500 cm$^{-1}$ after adsorption and photocatalysis indicates the important role of hydrogen bonds in adsorption and photocatalytic process. The adsorption of the amide groups on MIP-CuFeO$_2$@MnO$_2$ was also observed by XPS (Fig. 14b and c). The characteristic peaks of N 1 s appeared in MIP-CuFeO$_2$@MnO$_2$ at 399.8 eV is pyrrolic-N. After adsorption, the characteristic peak of N 1 s at 398.7 eV appeared, which was assigned as the N-H bond of the amide groups on the surface of the recovered catalyst.

The independent gradient model based on Hirshfeld partition (IGMH) method was also utilized to investigate the interaction of tetracycline with MIP-CuFeO$_2$@MnO$_2$ at the optimized geometric structure (at the left of Fig. 14d). In the IGMH map (at the right of Fig. 14d), the blue, green and red areas from IGMH map represent the prominent attractive weak interaction (H-bond, halogen-bond and purely ionic bond), van der Waals interaction and repulsive interaction



**Fig. 12.** (a) The *E. coli* growth curves in different liquid culture medium; (b) *E. coli* growth in different liquid culture medium for 24 h: (A) liquid culture medium, (B) liquid culture medium + TC solution, (C) liquid culture medium + degradation solution sampled at 30 min photocatalysis, (D) liquid culture medium + degradation solution sampled at 60 min photocatalysis, (E) liquid culture medium + degradation solution sampled at 90 min photocatalysis.
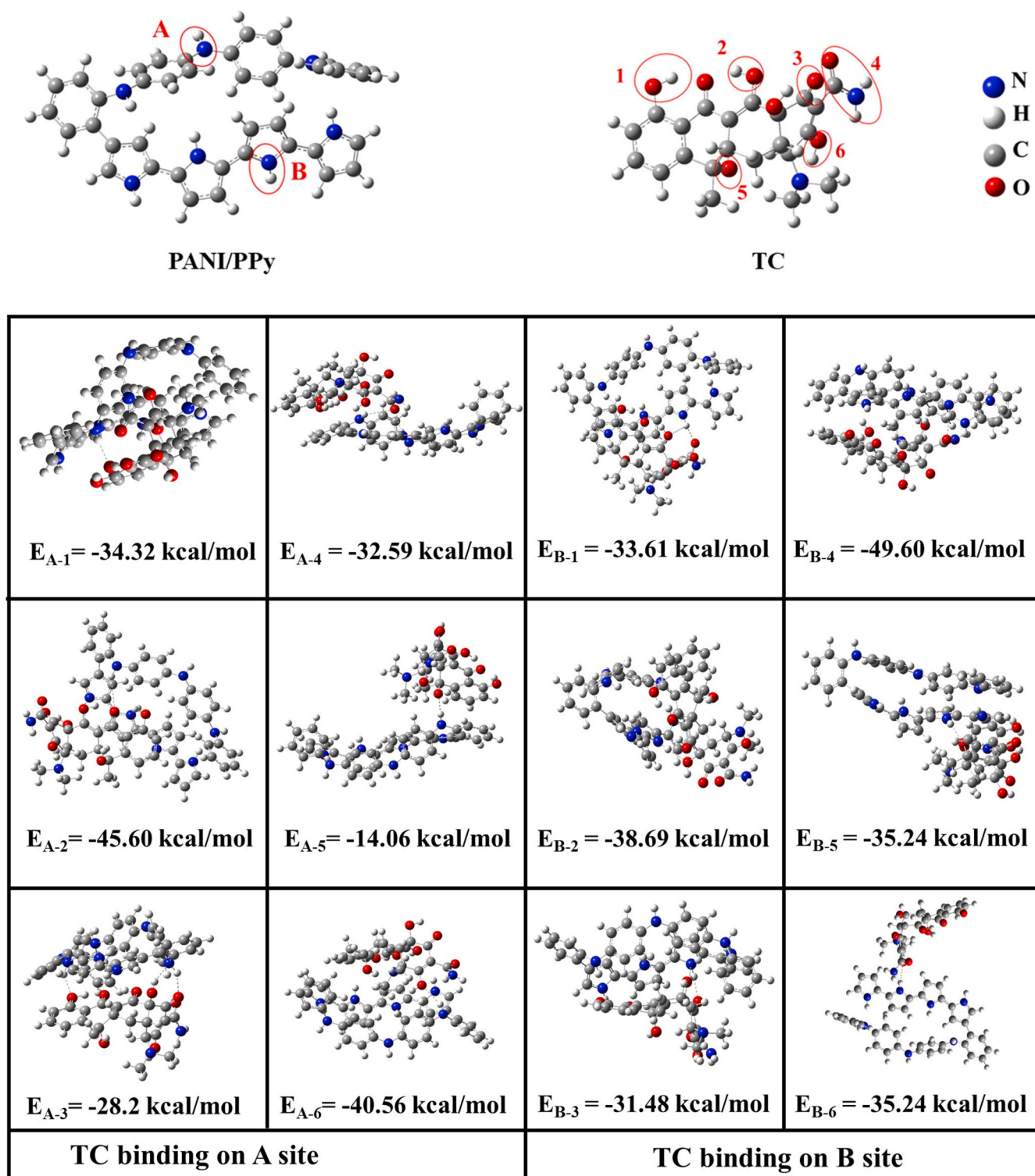
**Fig. 13.** Possible configurations of MIP-CuFeO$_2$@MnO$_2$ combined with TC and the interaction energy calculated from DFT calculation.

(steric effect in ring and cage), respectively. The interaction region between the tetracycline and imprinted copolymer layer of MIP-CuFeO$_2$@MnO$_2$ is mostly green, and the interaction region between the amide group of tetracycline and -NH- at site B of imprinted copolymer layer is blue, indicating van der Waals and hydrogen bond interactions.

The above analysis jointly confirms that the -NH- sites (A and B) are the main active sites on MIP-CuFeO$_2$@MnO$_2$, and MIP-CuFeO$_2$@MnO$_2$ exhibited recognition ability for amide groups of tetracycline. The

tetracycline was selectively recognized and adsorbed on the surface group-imprinted sites of copolymer layer via the hydrogen bond between amide groups of tetracycline and -NH- sites (A and B) of PANI/PPy copolymers.

According to the UV-Vis diffuse reflectance spectra, all the samples show strong visible-light absorption. Combined with Tauc plots and Mott-Schottky curves, the conduction band (CB), valence band (VB) and E$_g$ values of CuFeO$_2$ and MnO$_2$ were estimated (Fig. S9, Table S7).
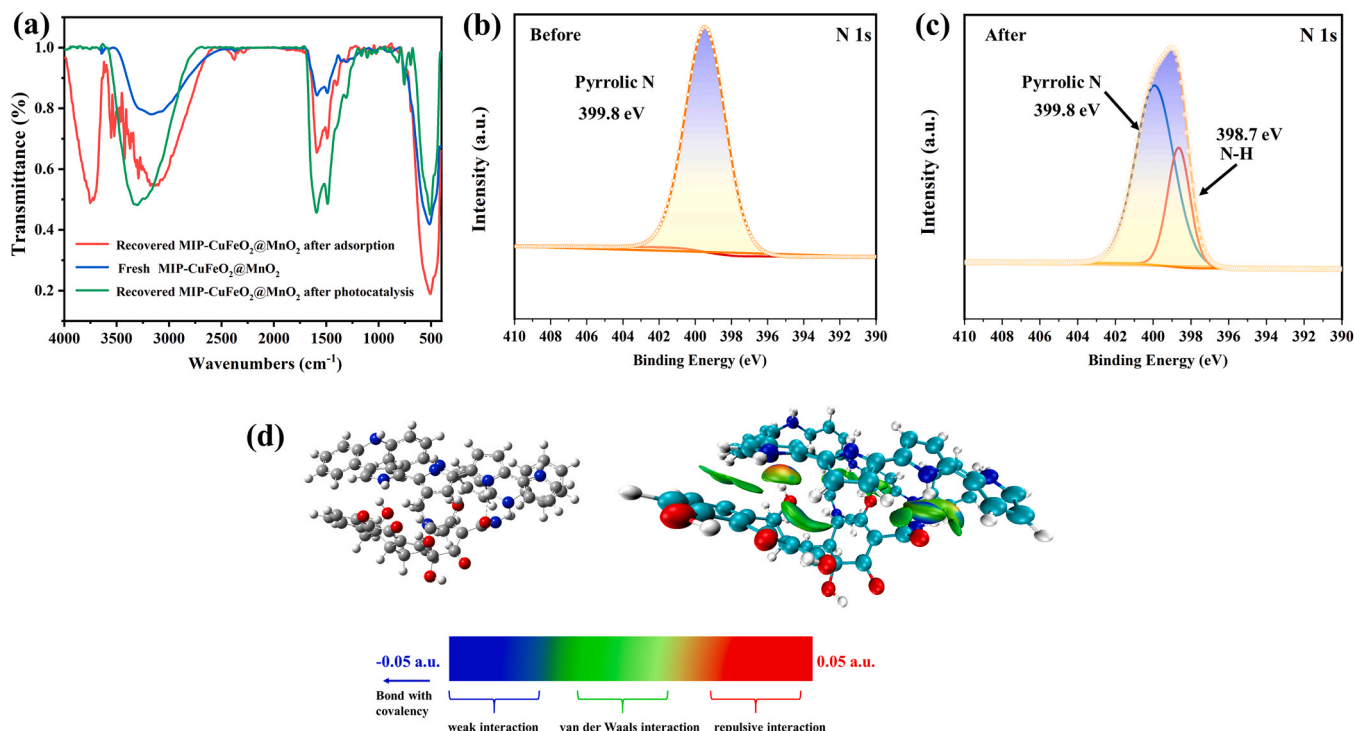
**Fig. 14.** (a) FT-IR of fresh and recovered MIP-CuFeO$_2$@MnO$_2$ after adsorption and photocatalytic reaction; High-resolution XPS of N 1 s in MIP-CuFeO$_2$@MnO$_2$ before (b) and after TC adsorption (c); The optimized geometric structure of the TC adsorption on MIP-CuFeO$_2$@MnO$_2$ (left) and corresponding IGMH diagram (right).

Moreover, the highest occupied molecular orbital (HOMO) and lowest unoccupied molecular orbital (LUMO) of PANI/PPy copolymer layer were obtained via DFT calculations (Fig. S10). According to the band structure and trapping experiment of reactive species, the photogenerated electrons (e$^-$) in LUMO of PANI/PPy copolymer moved into the CB of MnO$_2$ ($-0.759$ eV), and photogenerated holes (h$^+$) was transferred to HOMO of PANI/PPy. The separation and transfer of the photogenerated e$^-$ and h$^+$ between CuFeO$_2$ and MnO$_2$ follow by a direct Z-scheme path. Due to the CB of CuFeO$_2$ and MnO$_2$ are more negative than the O$_2$/O$_2^{\bullet-}$ redox potential (E = $-0.33$ eV), the photogenerated electrons can directly react with oxygen to generate superoxide radicals (O$_2^{\bullet-}$), and partial O$_2^{\bullet-}$ further reacted with H$_2$O to generate $^{\bullet}$OH radicals. The VB of CuFeO$_2$ and MnO$_2$, and the HOMO position ($-0.32$ eV) of PANI/PPy copolymer are lower than that of OH$^-$/$^{\bullet}$OH redox potential, thus the photogenerated h$^+$ cannot generate $^{\bullet}$OH radicals by oxidizing OH$^-$. The $^{\bullet}$OH, h$^+$ and O$_2^{\bullet-}$ radicals jointly participated in the
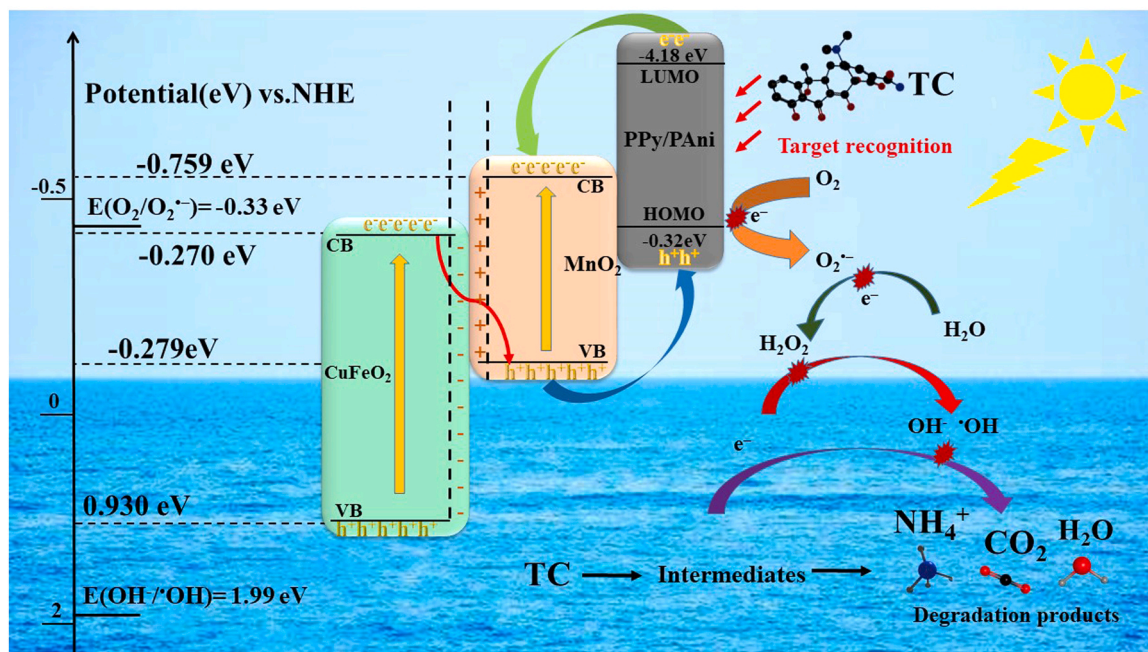


**Fig. 15.** The mechanism diagram of photocatalytic reaction.

preferential destruction of toxic groups in TC. The diagrammatic sketch of photocatalytic mechanism is shown in Fig. 15.

## 4. Conclusions

In summary, a group-imprinted MIP-CuFeO$_2$@MnO$_2$ as a novel heterogeneous photocatalyst was successfully fabricated using acrylamide as dummy templates for imprinting the amide group of tetracycline. After dummy molecular imprinting, the specific host-guest binding sites in the group-imprinted copolymer layer endowed MIP-CuFeO$_2$@MnO$_2$ with excellent specific recognition and preferential degradation performance for amide groups. MIP-CuFeO$_2$@MnO$_2$ exhibited higher adsorption capacity than the non-imprinted counterpart, and the adsorption isotherm followed by Langmuir model. The selection factor ($\alpha$) of MIP-CuFeO$_2$@MnO$_2$ is about 3.2 times that of non-imprinted counterpart in binary solution of tetracycline and ibuprofen, indicating the higher adsorption selectivity of MIP-CuFeO$_2$@MnO$_2$. The intermediates and degradation pathway of tetracycline by MIP-CuFeO$_2$@MnO$_2$ is different from that by the non-imprinted counterpart, and MIP-CuFeO$_2$@MnO$_2$ exhibited efficient targeted degradation performance of the amide group. Based on adsorption selectivity, degradation and DFT calculations, it can be concluded that imprinting effects make a substantial contribution to the specific recognition and preferential degradation of target chemical groups by the coupling technology of group-imprinting and photocatalysis.

## CRediT authorship contribution statement

**Junlong Peng**: Methodology, Data curation, Project administration. **Fang Deng:** Writing – original draft, Supervision. **Hongxin Shi**: Software. **Zhenzhou Wang**: Validation. **Xibao Li:** Writing – original draft. **Jianping Zou:** Writing – original draft, Writing – review & editing. **Xubiao Luo:** Writing – original draft, Writing – review & editing.

## Declaration of Competing Interest

The authors declare that they have no known competing financial interests or personal relationships that could have appeared to influence the work reported in this paper.

## Data Availability

Data will be made available on request.

## Acknowledgments

## Appendix A. Supporting information

Supplementary data associated with this article can be found in the online version at doi:10.1016/j.apcatb.2023.123179.

## References

[1] K.R. Davies, Y. Cherif, G.P. Pazhani, S. Anantharaj, H. Azzi, C. Terashima, A. Fujishima, S. Pitchaimuthu, The upsurge of photocatalysts in antibiotic micropollutants treatment: materials design, recovery, toxicity and bioanalysis, J. Photochem. Photobiol. C. 48 (2021) 100437, https://doi.org/10.1016/j.jphotochemrev.2021.100437.

[2] C.M. Oral, M. Ussia, M. Pumera, Hybrid enzymatic/Photocatalytic degradation of antibiotics via morphologically programmable light-driven ZnO microrobots, Small 18 (39) (2022), 2202600, https://doi.org/10.1002/smll.202202600.

[3] M. Bilal, S.S. Ashraf, D. Barceló, H.M. Iqbal, Biocatalytic degradation/redefining "removal" fate of pharmaceutically active compounds and antibiotics in the aquatic environment, Sci. Total Environ. 691 (2019) 1190–1211, https://doi.org/10.1016/j.scitotenv.2019.07.224.

[4] Q.A. Duong, L.F. Pittet, N. Curtis, P. Zimmermann, Antibiotic exposure and adverse long-term health outcomes in children: a systematic review and meta-analysis, J. Infect. 85 (2022) 213–300, https://doi.org/10.1016/j.jinf.2022.01.005.

[5] Y. Gu, J. Han, C. Jiang, Y. Zhang, Biomarkers, Oxidative stress and autophagy in skin aging, Ageing Res. Rev. 59 (2020), 101036, https://doi.org/10.1016/j.arr.2020.101036.

[6] X. Zhou, Z. Zhang, X. Liu, D. Wu, Y. Ding, G. Li, Y. Wu, Typical reactive carbonyl compounds in food products: formation, influence on food quality, and detection methods, Compr. Rev. Food Sci. Food Saf. 19 (2020) 503–529, https://doi.org/10.1111/1541-4337.12535.

[7] J. Liu, J. Li, Y. Li, J. Guo, S.M. Xu, R. Zhang, M. Shao, Photoelectrochemical water splitting coupled with degradation of organic pollutants enhanced by surface and interface engineering of BiVO$_4$ photoanode, Appl. Catal. B Environ. 278 (2020), 119268, https://doi.org/10.1016/j.apcatb.2020.119268.

[8] D. Lu, S. Xu, W. Qiu, Y. Sun, X. Liu, J. Yang, J. Ma, Adsorption and desorption behaviors of antibiotic ciprofloxacin on functionalized spherical MCM-41 for water treatment, J. Clean. Prod. 264 (2020) 121644, https://doi.org/10.1016/j.jclepro.2020.121644.

[9] L.N. Pincus, H.E. Rudel, P.V. Petrović, S. Gupta, P. Westerhoff, C.L. Muhich, J. B. Zimmerman, Exploring the mechanisms of selectivity for environmentally significant oxo-anion removal during water treatment: a review of common competing oxo-anions and tools for quantifying selective adsorption, Environ. Sci. Technol. 54 (2020) 9769–9790, https://doi.org/10.1021/acs.est.0c01666.

[10] D. Mangla, A. Sharma, S. Ikram, Critical review on adsorptive removal of antibiotics: present situation, challenges and future perspective, J. Hazard. Mater. 425 (2022), 127946, https://doi.org/10.1016/j.jhazmat.2021.127946.

[11] A. Yusuf, A. Sodiq, A. Giwa, J. Eke, O. Pikuda, G. De Luca, J.L. Di Salvo, S. Chakraborty, A review of emerging trends in membrane science and technology for sustainable water treatment, J. Clean. Prod. 266 (2020) 121867, https://doi.org/10.1016/j.jclepro.2020.121867.

[12] L. Issa, O. El Kik, M. El-Fadel, AnMBR technology for landfill leachate treatment: a framework towards improved performance, Rev. Environ. Sci. Biotechnol. 21 (2022) 517–538, https://doi.org/10.1007/s11157-022-09615-2.

[13] P.S. Goh, K.C. Wong, A.F. Ismail, Membrane technology: a versatile tool for saline wastewater treatment and resource recovery, Desalination 521 (2022), 115377, https://doi.org/10.1016/j.desal.2021.115377.

[14] A. Reza, L. Chen, Electrochemical treatment of livestock waste streams, Environ. Chem. Lett. 20 (2022) 1863–1865, https://doi.org/10.1007/s10311-022-01393-1.

[15] X.V. Medvedeva, J.J. Medvedev, S.W. Tatarchuk, R.M. Choueiri, A. Klinkova, Sustainable at both ends: electrochemical CO$_2$ utilization paired with electrochemical treatment of nitrogenous waste, Green. Chem. 22 (2020) 4456–4462, https://doi.org/10.1039/D0GC01754J.

[16] Y.L. Lin, N.Y. Zheng, H.C. Wang, Sludge dewatering through H$_2$O$_2$ lysis and ultrasonication and recycle for energy by torrefaction to achieve zero waste: an environmental and economical friendly technology, Renew. Sust. Energ. Rev. 155 (2022), 111857, https://doi.org/10.1016/j.rser.2021.111857.

[17] B. Chen, S. Zhou, N. Zhang, H. Liang, L. Sun, X. Zhao, J. Guo, H. Lu, Micro and nano bubbles promoted biofilm formation with strengthen of COD and TN removal synchronously in a blackened and odorous water, Sci. Total Environ. 837 (2022), 155578, https://doi.org/10.1016/j.scitotenv.2022.155578.

[18] J. Wang, X. Chen, Removal of antibiotic resistance genes (ARGs) in various wastewater treatment processes: an overview, Crit. Rev. Environ. Sci. Technol. 52 (2022) 571–630, https://doi.org/10.1080/10643389.2020.1835124.

[19] J. Peng, R. Yin, X. Yang, C. Shang, A novel UVA/ClO$_2$ advanced oxidation process for the degradation of micropollutants in water, Environ. Sci. Technol. 56 (2022) 1257–1266, https://doi.org/10.1021/acs.est.1c05133.

[20] W. Zhuang, Y. Zheng, J. Xiang, J. Zhang, P. Wang, C. Zhao, Enhanced hydraulic-driven piezoelectric ozonation performance by CNTs/BaTiO$_3$ nanocatalyst for Ibuprofen removal, Chem. Eng. J. 454 (2022), 139928, https://doi.org/10.1016/j.cej.2022.139928.

[21] A.M. Gorito, A.R.L. Ribeiro, P. Rodrigues, M.F.R. Pereira, L. Guimarães, C.M. R. Almeida, A.M. Silva, Antibiotics removal from aquaculture effluents by ozonation: chemical and toxicity descriptors, Water Res 218 (2022), 118497, https://doi.org/10.1016/j.watres.2022.118497.

[22] B. Yan, J. Peng, F. Deng, L. Liu, X. Li, P. Shao, J. Zou, S. Zhang, J. Wang, X. Luo, Novel ZnFe$_2$O$_4$/Bi$_2$S$_3$ high-low junctions for boosting tetracycline degradation and Cr(VI) reduction, Chem. Eng. J. 452 (2023), 139353, https://doi.org/10.1016/j.cej.2022.139353.

[23] T. Wu, X. Liu, Y. Liu, M. Cheng, Z. Liu, G. Zeng, B. Shao, Q. Liang, W. Zhang, Q. He, Application of QD-MOF composites for photocatalysis: energy production and environmental remediation, Coord. Chem. Rev. 403 (2020), 213097, https://doi.org/10.1016/j.ccr.2019.213097.

[24] J. Kosco, S. Gonzalez-Carrero, C.T. Howells, T. Fei, Y. Dong, R. Sougrat, G. Harrison, Y. Firdaus, R. Sheelamanthula, B. Purushothaman, F. Moruzzi, W. Xu, L. Zhao, A. Basu, S.D. Wolf, T. Anthopoulos, J.R. Durrant, I. McCulloch, Generation of long-lived charges in organic semiconductor heterojunction nanoparticles for efficient photocatalytic hydrogen evolution, Nat. Energy 7 (2022) 340–351, https://doi.org/10.1038/s41560-022-00990-2.

[25] F. Deng, J. Peng, X. Li, X. Luo, P. Ganguly, S.C. Pillai, B. Ren, L. Ding, D. D. Dionysiou, Metal sulfide-based Z-scheme heterojunctions in photocatalytic removal of contaminants, H$_2$ evolution and CO$_2$ reduction: current status and future perspectives, J. Clean. Prod. 416 (2023) 137957, https://doi.org/10.1016/j.jclepro.2023.137957.

[26] Z. Wang, D. Wang, F. Deng, X. Liu, X. Li, X. Luo, Y. Peng, J. Zhang, J. Zou, L. Ding, L. Zhang, Ag quantum dots decorated ultrathin g-C$_3$N$_4$ nanosheets for boosting degradation of pharmaceutical contaminants: insight from interfacial electric field induced by local surface plasma resonance, Chem. Eng. J. 463 (2023), 142313, https://doi.org/10.1016/j.cej.2023.142313.

[27] Q. Zhou, W. Huang, C. Xu, X. Liu, K. Yang, D. Li, Y. Hou, D.D. Dionysiou, Novel hierarchical carbon quantum dots-decorated BiOCl nanosheet/carbonized eggshell membrane composites for improved removal of organic contaminants from water via synergistic adsorption and photocatalysis, Chem. Eng. J. 420 (2021), 129582, https://doi.org/10.1016/j.cej.2021.129582.

[28] Y.R. Zheng, S. Hu, X.L. Zhang, H. Ju, Z. Wang, P.J. Tan, R. Wu, F.Y. Gao, T. T. Zhuang, X. Zheng, J.F. Zhu, M.R. Gao, S.H. Yu, Black phosphorous mediates surface charge redistribution of CoSe$_2$ for electrochemical H$_2$O$_2$ production in acidic electrolytes, Adv. Mater. 34 (2022), 2205414, https://doi.org/10.1002/adma.202205414.

[29] J.D. Lee, J.B. Miller, A.V. Shneidman, L. Sun, J.F. Weaver, J. Aizenberg, J. Biener, J.A. Boscoboinik, A.C. Foucher, A.I. Frenkel, J.E.S. van der Hoeven, B. Kozinsky, N. Marcella, M.M. Montemore, H.T. Ngan, C.R. O'Connor, C.J. Owen, D. J. Stacchiola, E.A. Stach, R.J. Madix, P. Sautet, C.M. Friend, Dilute alloys based on Au, Ag, or Cu for efficient catalysis: from synthesis to active sites, Chem. Rev. 122 (2022) 8758–8808, https://doi.org/10.1021/acs.chemrev.1c00967.

[30] T. Wang, J. Sun, Y. Hua, B.N.V. Krishna, Q. Xi, W. Ai, J.S. Yu, Planar and dendrite-free zinc deposition enabled by exposed crystal plane optimization of zinc anode, Energy Stor. Mater. 53 (2022) 273–304, https://doi.org/10.1016/j.ensm.2022.08.046.

[31] R. Yang, Y. Fan, R. Ye, Y. Tang, X. Cao, Z. Yin, Z. Zeng, MnO$_2$-based materials for environmental applications, Adv. Mater. 33 (2021), 2004862, https://doi.org/10.1002/adma.202004862.

[32] Y. Liu, Z. Jia, J. Zhou, G. Wu, Multi-hierarchy heterostructure assembling on MnO$_2$ nanowires for optimized electromagnetic response, Mater. Today Phys. 28 (2022), 100845, https://doi.org/10.1016/j.mtphys.2022.100845.

[33] Y. Wang, J. Yang, L. Wang, K. Du, Q. Yin, Polypyrrole/graphene/polyaniline ternary nanocomposite with high thermoelectric power factor, ACS Appl. Mater. Inter. 9 (2017) 20124–20131, https://doi.org/10.1021/acsami.7b05357.

[34] Q. Chen, H. Zhou, J. Wang, J. Bi, F. Dong, Activating earth-abundant insulator BaSO$_4$ for visible-light induced degradation of tetracycline, Appl. Catal. B Environ. 307 (2022), 121182, https://doi.org/10.1016/j.apcatb.2022.121182.

[35] S. Meng, Z. Nan, Rapid and selective adsorption of organic dyes with ultrahigh adsorption capacity using Na and Fe co-doped g-C$_3$N$_4$, Sep. Purif. Technol. 631 (2022), 121420, https://doi.org/10.1016/j.jcis.2022.11.006.

[36] L. Bi, Z. Chen, L. Li, J. Kang, S. Zhao, B. Wang, P. Yan, Y. Li, X. Zhang, J. Shen, Selective adsorption and enhanced photodegradation of diclofenac in water by molecularly imprinted TiO$_2$, J. Hazard. Mater. 407 (2021), 124759, https://doi.org/10.1016/j.jhazmat.2020.124759.

[37] I. Mahboob, I. Shafiq, S. Shafique, P. Akhter, M. Hussain, Y.K. Park, Effect of active species scavengers in photocatalytic desulfurization of hydrocracker diesel using mesoporous Ag$_3$VO$_4$, Chem. Eng. J. 441 (2022), 136063, https://doi.org/10.1016/j.cej.2022.136063.

[38] Q. Liu, S. Wang, F. Han, S. Lv, S. Yan, Y. Xi, J. Ouyang, Biomimetic tremelliform ultrathin MnO$_2$/CuO nanosheets on kaolinite driving superior catalytic oxidation: an example of CO, ACS Appl. Mater. Inter. 14 (2022) 44345–44357, https://doi.org/10.1021/acsami.2c11640.

[39] Y. Liu, X. Zhang, W. Zhang, X. Ge, Y. Wang, X. Zou, X. Zhou, W. Zheng, MXene-based quantum dots optimize hydrogen production via spontaneous evolution of Cl- to O-terminated surface groups, Energy Environ. Mater. (2022), https://doi.org/10.1002/eem2.12438.

[40] M. Xiao, Q. Wu, L. Li, S. Mu, M.N. Sørensen, W. Wang, C. Cui, Regenerable catalyst for highly alkaline water oxidation, ACS Energy Lett. 6 (2021) 1677–1683, https://doi.org/10.1021/acsenergylett.1c00127.

[41] R. Fiorenza, A. Di Mauro, M. Cantarella, C. Iaria, E.M. Scalisi, M.V. Brundo, A. Gulino, L. Spitaleri, G. Nicotra, S. Dattilo, S.C. Carroccio, V. Privitera, G. Impellizzeri, Preferential removal of pesticides from water by molecular imprinting on TiO$_2$ photocatalysts, Chem. Eng. J. 379 (2020), 122309, https://doi.org/10.1016/j.cej.2019.122309.

[42] M. Zambrzycki, R. Piech, S.R. Raga, M. Lira-Cantu, A. Fraczek-Szczypta, Hierarchical carbon nanofibers/carbon nanotubes/NiCo nanocomposites as novel highly effective counter electrode for dye-sensitized solar cells: a structure-electrocatalytic activity relationship study, Carbon 203 (2023) 97–110, https://doi.org/10.1016/j.carbon.2022.11.047.

[43] Y. Liu, X. Zhang, W. Zhang, X. Ge, Y. Wang, X. Zou, X. Zhou, W. Zheng, MXene-based quantum dots optimize hydrogen production via spontaneous evolution of Cl-to O-terminated surface groups, Energy Environ. Mater. (2022), e12438, https://doi.org/10.1002/eem2.12438.

[44] F.R. Praxedes, M.A. Nobre, P.S. Poon, J. Matos, S. Lanfredi, Nanostructured KxNa1-xNbO$_3$ hollow spheres as potential materials for the photocatalytic treatment of polluted water, Appl. Catal. B Environ. 298 (2021), 120502, https://doi.org/10.1016/j.apcatb.2021.120502.

[45] X. Wang, B. Cheng, L. Zhang, J. Yu, I. Normatov, Adsorption performance of tetracycline on NiFe layered double hydroxide hollow microspheres synthesized with silica as the template, J. Colloid Interf. Sci. 627 (2022) 793–803, https://doi.org/10.1016/j.jcis.2022.07.063.

[46] H. Jia, W. He, W.G. Wamer, X. Han, B. Zhang, S. Zhang, Z. Zheng, Y. Xiang, J. J. Yin, Generation of reactive oxygen species, electrons/holes, and photocatalytic degradation of rhodamine B by photoexcited CdS and Ag$_2$S micro-nano structures, J. Phys. Chem. C. (37) (2014) 21447–21456, https://doi.org/10.1021/jp505783y.

[47] Y. Wang, H. Zhang, J. Zhang, C. Lu, Q. Huang, J. Wu, F. Liu, Degradation of tetracycline in aqueous media by ozonation in an internal loop-lift reactor, J. Hazard. Mater. 192 (2011) 35–43, https://doi.org/10.1016/j.jhazmat.2011.04.086.